

Equivalent Near-Field Corner Frequency Analysis of 3D Dynamic Rupture Simulations Reveals Dynamic Source Effects

Nico Schliwa^{*1} and Alice-Agnes Gabriel^{1,2}

Abstract

Dynamic rupture simulations generate synthetic waveforms that account for nonlinear source and path complexity. Here, we analyze millions of spatially dense waveforms from 3D dynamic rupture simulations in a novel way to illuminate the spectral fingerprints of earthquake physics. We define a Brune-type equivalent near-field corner frequency (f_c) to analyze the spatial variability of ground-motion spectra and unravel their link to source complexity. We first investigate a simple 3D strike-slip setup, including an asperity and a barrier, and illustrate basic relations between source properties and f_c variations. Next, we analyze > 13,000,000 synthetic near-field strong-motion waveforms generated in three high-resolution dynamic rupture simulations of real earthquakes, the 2019 M_w 7.1 Ridgecrest mainshock, the M_w 6.4 Searles Valley foreshock, and the 1992 M_w 7.3 Landers earthquake. All scenarios consider 3D fault geometries, topography, off-fault plasticity, viscoelastic attenuation, and 3D velocity structure and resolve frequencies up to 1–2 Hz. Our analysis reveals pronounced and localized patterns of elevated f_c , specifically in the vertical components. We validate such f_c variability with observed near-fault spectra. Using isochrone analysis, we identify the complex dynamic mechanisms that explain rays of elevated f_c and cause unexpectedly impulsive, localized, vertical ground motions. Although the high vertical frequencies are also associated with path effects, rupture directivity, and coalescence of multiple rupture fronts, we show that they are dominantly caused by rake-rotated surface-breaking rupture fronts that decelerate due to fault heterogeneities or geometric complexity. Our findings highlight the potential of spatially dense ground-motion observations to further our understanding of earthquake physics directly from near-field data. Observed near-field f_c variability may inform on directivity, surface rupture, and slip segmentation. Physics-based models can identify “what to look for,” for example, in the potentially vast amount of near-field large array or distributed acoustic sensing data.

Cite this article as Schliwa, N., and A.-A. Gabriel (2023). Equivalent Near-Field Corner Frequency Analysis of 3D Dynamic Rupture Simulations Reveals Dynamic Source Effects, *Seismol. Res. Lett.* **95**, 900–924, doi: [10.1785/0220230225](https://doi.org/10.1785/0220230225).

[Supplemental Material](#)

Introduction

The advances of seismic array analysis (e.g., Rost and Thomas, 2002; Dougherty *et al.*, 2019; Arrowsmith *et al.*, 2022), the rise of distributed acoustic sensing (DAS, e.g., Zhan, 2019) and detailed displacement analysis using high-rate Global Navigation Satellite Systems networks (e.g., Madariaga *et al.*, 2019; Paziewski *et al.*, 2020) highlight the potential of dense ground-motion observations. Near-field recordings of well-instrumented earthquakes (Sieh *et al.*, 1993; Chung and Shin, 1999; Langbein *et al.*, 2005; Ross *et al.*, 2019) have revealed large variability of ground motions, which may originate from local site, path, and source effects (Shakal *et al.*, 2006; Ripperger *et al.*, 2008). For example, Olsen *et al.* (2008) report

“star burst patterns” of increased ground-motion peak values radiating out from the San Andreas fault where a dynamic rupture pulse changes abruptly in either speed, direction, or shape.

Concurrently, numerical forward simulations of earthquakes, combining realistic modeling of seismic sources and wave propagation, have advanced tremendously over the last decades and can provide realistic and spatially dense ground-

1. Department of Earth and Environmental Sciences, Ludwig-Maximilians Universität München, Munich, Germany, <https://orcid.org/0009-0004-7825-9458> (NS); <https://orcid.org/0000-0003-0112-8412> (A-AG); 2. Scripps Institution of Oceanography, UC San Diego, La Jolla, California, U.S.A.

*Corresponding author: nico.schliwa@geophysik.uni-muenchen.de

© Seismological Society of America

motion synthetics. Earthquakes on prescribed finite-fault geometries are modeled using kinematic (Ben-Menahem, 1962; Haskell, 1964) or dynamic (Andrews, 1976; Madariaga, 1976) approaches. Kinematic models prescribe coseismic slip evolution and are computationally more efficient but do not guarantee a physically consistent source description (e.g., Tinti *et al.*, 2005). Dynamic rupture models provide mechanically viable descriptions of how faults yield and slide based on laboratory-derived friction laws and can provide physics-based correlations among macroscopic earthquake rupture parameters, such as slip rate and rupture time (Grueter *et al.*, 2004; Schmedes *et al.*, 2010; Savran and Olsen, 2020; Vyas *et al.*, 2023). High-performance computing allows deterministic modeling of the broadband seismic wavefield in the near field of kinematic and dynamic earthquake models across the bandwidth of relevance for earthquake engineering (e.g., Heinecke *et al.*, 2014; Withers *et al.*, 2018; Rodgers *et al.*, 2019; Taufiqurrahman *et al.*, 2022). A high degree of realism of 3D physics-based forward simulations can be achieved by integrating observational data sets, such as high-resolution velocity structure and topography (e.g., Small *et al.*, 2017; Pitarka *et al.*, 2021), as well as physically relevant mechanisms beyond elasticity and simple source geometries, such as fault zone plasticity, viscoelastic attenuation, and fault roughness and segmentation (e.g., Shi and Day, 2013; Roten *et al.*, 2017; Wollherr *et al.*, 2019; Li, Gabriel, *et al.*, 2023; Taufiqurrahman *et al.*, 2023).

Various connections between earthquake source complexity and the variability of observed and modeled strong ground motions have been identified. Surface breaking of dynamic rupture can cause large fault-parallel ground velocity pulses (Kaneko and Goto, 2022). High-frequency and high-intensity radiation that dominates ground acceleration can be generated by abrupt changes in rupture velocity, heterogeneity of slip or slip rate, or variations in fault geometry (Madariaga, 1977, 1983; Spudich and Cranswick, 1984; Hartzell *et al.*, 1996; Madariaga *et al.*, 2006; Shi and Day, 2013). Small-scale ruptures in laboratory experiments and large earthquakes analyzed using backprojection emit high-frequency radiation close to the rupture tip (e.g., Marty *et al.*, 2019; Li *et al.*, 2022). Pulido and Dalguer (2009) analyzed the high-frequency radiation of large stress-drop regions (“asperities”) and areas with a larger strength excess than their surroundings (“barriers”). They found that most of the high-frequency radiation during the 2000 Tottori earthquake originated from only 20% of the total asperity area, thereby highlighting the local character of the generating mechanism(s). Envelope inversions of ground accelerations show that high-frequency waves radiate mainly near the periphery of the fault plane or at the boundary of large slip areas (Zeng *et al.*, 1993; Kakehi and Irikura, 1996). Using a hybrid backprojection method, Okuwaki *et al.* (2014) observed that strong high-frequency radiation precedes the large asperity rupture of the 2010 M_w 8.8 Chile earthquake.

Recent observational data analyses imply that high-frequency radiation may strongly correlate with fault trace “misalignment” (Chu *et al.*, 2021), that is, geometric fault complexity. Adda-Bedia and Madariaga (2008) showed theoretically that a rupture front turning at a fault kink generates a burst of high-frequency radiation aligned with a jump in particle velocity, which has also been observed in 3D dynamic and kinematic rupture simulations (Oglesby and Mai, 2012; Li *et al.*, 2022). Zhang and Ge (2017) reported peaks in high- and low-frequency seismic energy release at a stepover rupture during the 2014 M_w 7.0 Yutian earthquake. Dynamic rupture models of stepover faults (e.g., Lozos *et al.*, 2014) show high-frequency peak ground velocity bursts radiating beyond the slipping faults (Hu *et al.*, 2018). While rupture directivity affects dominantly low- and intermediate-frequency bands, it can cause most of the seismic energy from a finite rupture to arrive as a single large pulse and may increase the components’ average high-frequency radiation in a magnitude-dependent frequency band (Somerville *et al.*, 1997; Kane *et al.*, 2013). The strength of directivity effects depends on the ratio of the mean rupture velocity to wave propagation velocity (Boore and Joyner, 1978). 3D dynamic rupture simulations have shown that off-fault plasticity causes near-fault peak ground velocities to saturate and increases the dominant period of such a directivity pulse (Wang and Day, 2020).

However, identifying and physically interpreting observable near-field ground-motion complexities remains challenging. Theoretical source models often assume simple, for example, circular, source geometries, and a constant subshear/sub-Rayleigh rupture speed. Dynamic rupture simulations have demonstrated that this is rarely the case for large earthquakes (e.g., Ulrich, Gabriel, *et al.*, 2019; Ulrich, Vater, *et al.*, 2019; Harris *et al.*, 2021; Yu *et al.*, 2022; Jia *et al.*, 2023). Recent observational studies show that also small events exhibit considerable rupture complexity and that their spectra often deviate from simple circular (ω^2 decay) source models (e.g., Fan and McGuire, 2018; Pennington *et al.*, 2023; Yoshida and Kanamori, 2023). But even for the best-recorded earthquakes, observations often miss the spatial resolution required to uniquely relate ground-motion variability to source complexity.

Here, we aim to systematically relate the spectral properties of synthetic strong ground motions from 3D dynamic rupture earthquake scenarios to physics-based source complexity. We analyze millions of synthetic waveforms from dynamic rupture simulations to illuminate the spectral fingerprints of earthquake source mechanisms in the near field. We define a spatially variable Brune-type (Brune, 1970) corner frequency f_c as a scalar proxy of a waveform’s relative frequency content to analyze its variability in the vicinity of rupturing fault systems and associate it with different aspects of source complexity. We term f_c as the equivalent near-field corner frequency to avoid any confusion with far-field corner frequency analysis. We

analyze four 3D dynamic rupture models of increasing complexity for which we generate spatially high-resolution ground-motion synthetic seismograms. We identify distinct spatial patterns in f_c that are associated with fault geometry complexity, rupture directivity, surface rupture, or variable slip distribution. We use isochrone theory (Bernard and Madariaga, 1984; Spudich and Cranswick, 1984) to locate the sources of high-frequency radiation and to interpret our results.

Methods

Equivalent near-field corner frequency

The average corner frequency of far-field source spectra can be used to estimate an event's stress drop (e.g., Brune, 1970; Thatcher and Hanks, 1973; Allmann and Shearer, 2009; Abercrombie, 2021), which requires a theoretical model of the source. The classical Brune (1970) model describes the displacement amplitude spectrum $A(f)$ of far-field body waves as follows:

$$A(f) = \frac{\Omega_0}{1 + (f/f_c)^2}, \quad (1)$$

in which Ω_0 is the amplitude of the lowest frequency of the spectrum; f_c is the corner frequency; and f is a well-defined frequency band. The Brune-type spectrum is flat at low frequencies, with Ω_0 proportional to the seismic moment M_0 , and it has an ω^{-2} fall-off rate at high frequencies. The corner frequency f_c marks the transition between the two parts of the spectrum.

In this study, we aim to analyze the relative spatial variability of simulated spectra in the near field in distinction to inferring source properties, such as source dimensions or stress drop. Although we model not exclusively the near field, we focus on near-field effects (see Appendix). In all our models, the respective S -wave travel times from the slipping faults to the model domain boundaries correspond to 2–3 times the respective rupture duration. We adapt the classical Brune (1970) model (equation 1) to determine near-field spectral corner frequencies. We acknowledge that our application violates some of Brune (1970) underlying theoretical assumptions: our simulated waveforms include nonnegligible near-field terms, the effects of topography and 3D velocity structure, and a clear separation between P - and S -wave spectra is mostly impossible because the event durations are longer than the arrival-time differences (e.g., Madariaga *et al.*, 2019). Thus, we term the inferred spectral waveform property the equivalent near-field corner frequency (f_c).

First, we rotate the horizontal components of all synthetic seismograms into radial and transverse components with respect to the absolute slip centroid of the respective dynamic rupture model. We then apply a tapered body-wave window to each time series to mitigate the impact of later arriving surface waves. The body-wave window effect is generally small, except

in the Searles Valley dynamic rupture simulation. The body-wave window starts at the P -wave arrival time. Its length is chosen as the rupture duration of the respective dynamic rupture scenario added to an S -wave delay specifically calculated for each virtual station based on its distance to the slip centroid. Notably, using this body-wave window prevents a deflected high f_c ray in the Searles Valley foreshock dynamic rupture scenario from affecting our analysis. In other scenarios, its effect is negligible. With this approach, we disregard time-dependent frequency content and focus our analysis on spatial variability.

Next, we Fourier transform the velocity waveforms and integrate the spectra by division with $i\omega$. The order of these operations is important because computing the Fourier transform of an already integrated displacement time series, which potentially contains static displacement and is thus not periodic, can lead to spectra that are contaminated at all frequencies (Madariaga *et al.*, 2019). In the next step, we resample the spectrum to equally spaced sampling points up to the numerically resolved maximum frequency of each simulation (see Appendix). An alternative approach would be to resample the spectrum to a logarithmic spacing (e.g., Ide *et al.*, 2003).

We solve equation (1) for all possible f_c values in 0.005 Hz steps between the inverse of the body-wave window (always <0.1 Hz) and 1.0 Hz and evaluate the misfits between the simulated and analytical spectra. We define the equivalent near-field corner frequency as the value of all possible f_c values, which leads to the smallest misfit. Theoretically, Ω_0 in equation (1) is given by the amplitude of the lowest frequency of the respective spectrum. However, the fit can be generally improved by considering a mean amplitude value of the low-frequency part (e.g., Trugman, 2020). Here, we choose the mean value of the lowest frequency up to the respective f_c , which renders our approach robust for spectra that contain static displacements and are not flat at the low-frequency part (e.g., station CLC in Fig. S5, available in the supplemental material to this article). This approach differs from the classical Brune model in which the amplitude is half of the long-period level at f_c . However, this does not lead to a systematic underestimation at long-period levels (Figs. S5 and S6).

We use the spectral seismological misfit approach of Karimzadeh *et al.* (2018) for corner frequency picking:

$$\text{Misfit}_{\text{ss}} = \frac{1}{n_f} \sum_{i=1}^n \left| \log \frac{A(f_i)}{A_{\text{Brune}}(f_i)} \right|, \quad (2)$$

in which f_i are the discrete sample points of the spectra; and n_f is the absolute number of sample points. $A(f_i)$ are the spectral amplitudes of the synthetic waveforms and $A_{\text{Brune}}(f_i)$ are the amplitudes of the respective Brune-type spectra (equation 1). This approach has two major benefits compared with a root mean square misfit. It is based on relative differences and, therefore, is independent of the examined absolute amplitudes.

In addition, its logarithmic scaling prevents overweighting of outliers in strongly oscillating spectra (e.g., [Lindley and Archuleta, 1992](#)).

We compute f_c using parallelized Python code and exploiting efficient NumPy tensor operations ([Harris et al., 2020](#)). We openly provide our code (see [Data and Resources](#)) that automatically facilitates the loading of raw waveform data, preprocessing, and calculation of f_c . For example, our script requires ~ 23 min to process 3,000,000 waveforms of the Landers earthquake dynamic rupture scenario using 30 processes. Input data loading is also parallelized but does not optimally scale and uses $\sim 50\%$ of the computational runtime. We perform the computations on an AMD EPYC 7662 64-Core processor with a 2 GHz clock speed.

Isochrone theory

We use isochrone theory ([Bernard and Madariaga, 1984](#); [Spudich and Frazer, 1984](#)) to interpret the equivalent near-field corner frequency distributions. Isochrone theory assumes that close to large earthquakes, most high-frequency ground motions are caused by direct P and S waves generated at the rupture front ([Madariaga, 1983](#); [Spudich and Cranswick, 1984](#); [Marty et al., 2019](#)). Under this assumption, high-frequency ground motions recorded at a station can be derived from a series of line integrals instead of using the full surface integral of the representation theorem.

In the framework of isochrone theory, the integration path for each time step consists only of points on the fault associated with the high-frequency radiation that arrives at the observer at the respective time step. These lines are called isochrones and are contour lines of the sum of the rupture times and travel times to the respective station. Rupture time is defined as the time at which the absolute slip rate at a point on the fault exceeds 0.001 m/s. The ground velocities can be directly related to the isochrone velocity c , which is proportional to the isochrone spacing as follows:

$$c(x, z, \underline{r}) = |\nabla_s t(x, z, \underline{r})|^{-1}, \quad (3)$$

and ∇_s is the surface gradient with respect to the fault coordinates (x, z) ; t is the isochrone time (the sum of the rupture time and travel time); and \underline{r} are the coordinates of the station. Points on the fault in which c is singular radiate particularly high frequencies. A prominent example is supershear rupture and its associated S -wave Mach cones ([Spudich and Frazer, 1984](#)). Spatial variations in the slip velocity and temporal variations in the isochrone velocity can cause comparable ground accelerations. Seismic directivity decreases isochrone spacing, thereby increasing isochrone velocity ([Spudich and Chiou, 2008](#)). Thus, isochrone analysis inherently captures the contributions of near-field directivity effects.

To use isochrone theory to analyze complex dynamic rupture scenarios, here, we mostly use the peak slip-rate time

instead of the rupture (initiation) time. Peak slip-rate time is also associated with the rupture front but is often smoother and less prone to ambiguity, for example, due to multiple rupture (and healing) fronts. We only assign peak slip-rate times to points on the fault where the peak slip rate exceeds 0.05 m/s for TPV5 and 0.1 m/s for the Ridgecrest and Landers dynamic rupture models. In the following, we mostly show peak slip-rate times inferred from the dip-slip components to separate the vertical slip from the strike-parallel slip and to isolate the effects of rake-rotated rupture fronts.

Results

We analyze the waveforms generated in 3D dynamic rupture simulations of a simple community benchmark setup and three large-scale scenarios of real earthquakes. All four dynamic rupture scenarios are detailed in the [Appendix](#). In the following, “high-frequency” refers to frequencies higher than approximately twice the inverse of the event duration, which is 0.22 Hz for the community benchmark TPV5, 0.2 Hz for the Searles Valley foreshock, 0.14 Hz for the Ridgecrest mainshock, and 0.11 Hz for the Landers earthquake dynamic rupture scenarios. For the latter, we exclude the last and smallest subevent on the Camp Rock fault in this approximation, which increases rupture duration but contributes weakly to the seismic moment.

TPV5 3D dynamic rupture community benchmark

We demonstrate the relationship between the source properties, high-frequency radiation, and equivalent near-field corner frequency variations using the TPV5 U.S. Geological Survey / Southern California Earthquake Center (USGS/SCEC) 3D dynamic rupture community benchmark ([Harris et al., 2009](#)). The benchmark’s domain is a homogeneous elastic half-space; therefore, no path or site effects affect our analysis. We model a bilateral strike-slip dynamic rupture passing an asperity and a barrier, regions with elevated or reduced initial shear stresses, which significantly accelerate or decelerate the rupture, respectively (Fig. 1d).

Figure 1e–h shows two pairs of isochrone contours on the fault plane and acceleration waveforms of the respective virtual stations. Isochrones in Figure 1e are calculated by adding the S -wave travel time at station T1 (located at $x = -10$ km and $y = 30$ km; Fig. 1b) to the rupture time. The patch in the middle represents the overstressed nucleation area. The rupture acceleration due to the left asperity causes an increased isochrone spacing to the left side of the hypocenter and vice versa the rupture deceleration due to the right barrier causes a decrease in isochrone spacing to the right side of the hypocenter. Figure 1f shows the corresponding acceleration time series of the transverse component at T1. Ground accelerations are generally associated with high-frequency radiation and are proportional to changes in the isochrone spacing ([Spudich and Frazer, 1984](#)). Every pronounced high-amplitude signal in the accelerogram can be related to a specific rupture

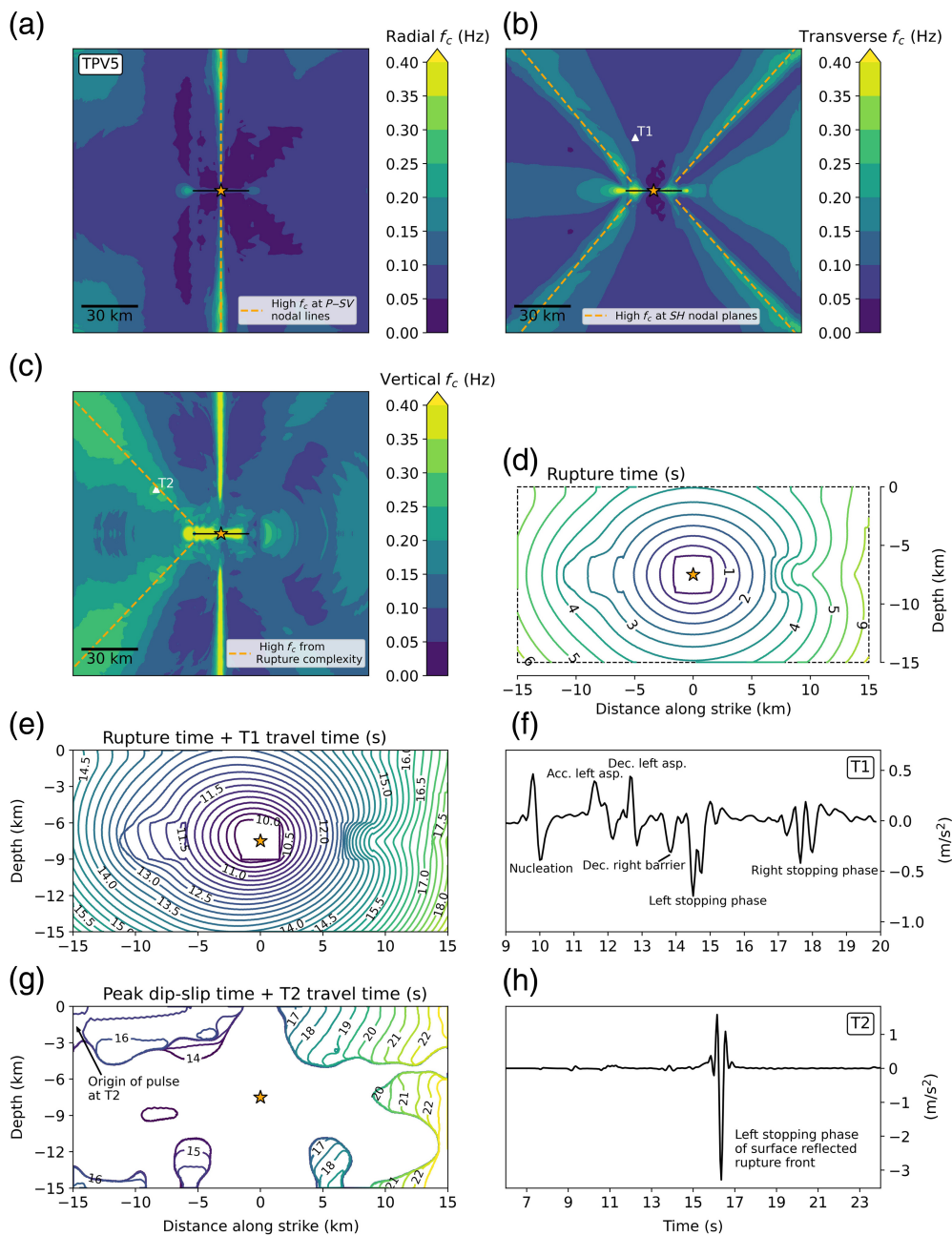
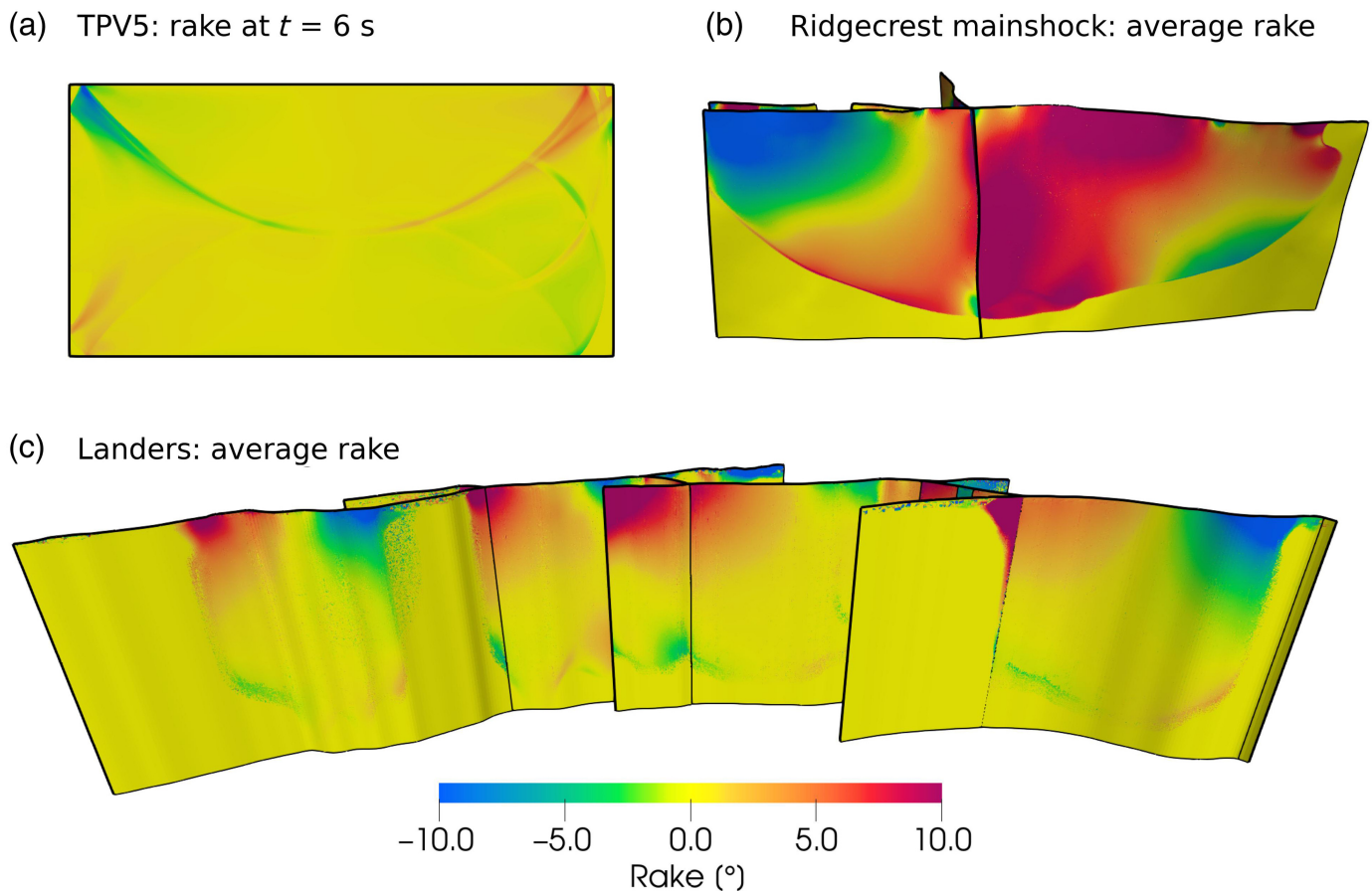


Figure 1. TPV5's equivalent near-field corner frequency (f_c) distribution of the (a) radial, (b) transverse, and (c) vertical components of synthetic seismograms recorded at $\sim 900,000$ virtual seismic stations in map view. The seismograms are generated in a bilateral strike-slip 3D dynamic rupture model including an asperity and a barrier embedded in a homogeneous elastic half-space (the TPV5 Southern California Earthquake Center [SCEC]/U.S. Geological Survey [USGS] community benchmark, [Harris et al., 2009](#)). The black lines indicate the fault trace, the star marks the hypocenter, and white triangles are stations that are analyzed in panels (e–h). The orange lines mark different high- f_c features. (d) Side-view of the fault plane with rupture front contours in 0.5 s intervals. (e) Isochrone contours of station T1 in 0.5 s intervals. (f) Transverse ground accelerations at station T1. Comparison with isochrones allows associating pronounced high-amplitude signals with different stages of 3D dynamic rupture propagation. Acc., acceleration; dec., deceleration; asp., asperity. (g) Peak dip-slip isochrone contours of station T2 in 0.5 s intervals. (h) Vertical ground accelerations at station T2. The color version of this figure is available only in the electronic edition.

phase by comparing the time step with the respective isochrone. For example, the acceleration oscillations at 10 s are caused by the nucleation, the two spikes at 11.5 and 12.5 s represent the acceleration and deceleration at the high-stress asperity, and the strongest pulse at 14.5 s results from stopping phases when rupture reaches the prescribed left end of the fault.

Figure 1g shows the peak dip-slip isochrones (the sum of the S-wave travel time and peak dip-slip time) at station T2 (located at $x = -35$ km and $y = 25$ km; Fig. 1c). Those points on the fault with peak dip-slip rates of less than 0.05 m/s are ignored because their contribution to the radiated waves is negligible. We use a median filter favoring the dominant isochrones to avoid oscillations in which different rupture fronts have a comparable peak slip rate. Figure 1h shows the vertical ground accelerations at station T2, which are dominated by a single spike shortly after 16 s. Isochrone analysis reveals that this spike is caused by a phase of dip-slip acceleration and abrupt rupture arrest induced by a surface-reflected rupture front. The large isochrone spacing (after 16 s, Fig. 1g) at the upper left side of the fault shows this strongly accelerating dip-slip phase that abruptly stops at the left fault end. The dip-slip phase originates from rake rotation at the dynamic rupture front, which is larger at shallow depths and is significantly amplified when the rupture breaks the surface ([Oglesby et al., 2000](#)). Such shallow rake rotation has been linked to geological features



such as slickenlines (Kearse and Kaneko, 2020) and increased tsunami hazards of strike-slip fault systems (Kutschera *et al.*, 2023; Li, Gabriel, *et al.*, 2023).

Important, the equivalent near-field corner frequency f_c is not a direct measure of the high-frequency content of the modeled seismic wavefield but rather reflects a relative association between high and low frequencies. Figure 1a–c shows the f_c distribution of the radial, transverse, and vertical components of the synthetic seismograms recorded at $\sim 900,000$ virtual stations in map view. We observe pronounced variability in f_c . A thin ray of high f_c in fault-normal direction, visible in the radial and vertical components (Fig. 1a,c), reflects the nodal line of the P – SV radiation pattern and is also present in other corner frequency studies of (near) symmetrical ruptures (e.g., Kaneko and Shearer, 2015; Wang and Day, 2017) and in spectral estimates using data of the Large- n seismic survey in Oklahoma (LASSO; Kemna *et al.*, 2020).

Rays of high f_c form in the transverse components (Fig. 1b) at an angle of $\sim 45^\circ$ to the rupture propagation direction. These reflect the nodal planes of a strike-slip SH radiation pattern centered at the hypocenter. The radiation pattern affects low frequencies stronger than high frequencies (e.g., Takemura *et al.*, 2009; Trugman *et al.*, 2021), which leads to a lack of low-frequency energy at the nodal planes and thus locally increases the measured f_c .

Figure 2. (a) Rake at $t = 6$ s of the TPV5 dynamic rupture model (Harris *et al.*, 2009). (b) Average rake of the 2019 M_w 7.1 Ridgecrest mainshock dynamic rupture model (Taufiqurrahman *et al.*, 2023). (c) Average rake of the 1992 M_w 7.3 Landers dynamic rupture model (Wollherr *et al.*, 2019). The color version of this figure is available only in the electronic edition.

We observe two raylike high- f_c patterns at approximately the same 45° angle to the fault trace in the vertical components (Fig. 1c), for example, where station T2 is placed. We link these to the high-amplitude lobes of a strike-slip P – SV radiation pattern in the rupture-forward direction of a vertical high-frequency pulse caused by a rapidly accelerating and decelerating phase of dip-slip during surface-breaking rupture, as shown in the isochrones in Figure 1g. We quantify the rake rotation related to shallow dip-slip to be only up to 10° (Fig. 2a). Thus, the overall radiation is dominated by the strike-slip radiation pattern. Directivity effects additionally sharpen the vertical ground-motion pulse and contribute to the high f_c . The vertical-component high- f_c bands are of considerably lower amplitudes on the right side of the model domain. This is caused by the differences in bending of the rupture front due to either high- or low-shear stress patches (Fig. 1d). Convex bending due to the submerged left, high-shear stress asperity leads to more abrupt decelerating of the surface-reflected rupture front, generating more high-frequency radiation.

2019 Ridgecrest sequence

We analyze the relationship between the equivalent near-field corner frequency f_c , isochrones, and source complexity in [Taufiqurrahman et al. \(2023\)](#) 3D dynamic rupture scenario for the 2019 M_w 7.1 Ridgecrest mainshock. We also analyze the f_c distribution of their Searles Valley foreshock dynamic rupture model, which reveals additional path effects. In the following, we refer to the dominant impact of the 3D velocity structure as “path effects” and not to the effects of the also modeled intrinsic viscoelastic attenuation, which may become more relevant at higher frequencies than considered here. We do not include (nonlinear) site effects in our models ([Hu et al., 2021](#); [Roten et al., 2023](#)) as the surface S-wave velocities considered in our models are mostly higher than 1.5 km/s (with exceptions being the Salton Sea basin and the San Bernardino basin in the Landers model), and elastic moduli do not change due to the passage of seismic waves (e.g., [Niu et al., 2023](#)). Figure 3 provides an overview of both dynamic rupture models, and the [Appendix](#) includes a detailed description.

The Ridgecrest mainshock dynamic rupture scenario ruptures primarily along a northwest–southeast-trending continuous fault (F3 in Fig. 3c). The rupture starts as a bilateral crack that expands away from the hypocenter. After 5 s rupture time, it terminates to the north due to a locally lower prestress and a less optimal fault orientation. The southward rupture cannot break through the conjugate F2–F3 intersection at shallow depths due to the stress shadow caused by the foreshock dynamic rupture scenario ([Taufiqurrahman et al., 2023](#)). Only deep decelerated slip “tunnels” the intersection and regrows as a pulse that ruptures again to the surface and to the southeastern end of F3.

Figure 4 shows the f_c distribution of the three components of the Ridgecrest mainshock dynamic rupture simulation, complemented by a map of the regional topography incorporated into the model and the fault system surface traces. For each component, the equivalent near-field corner frequencies are computed at $\sim 1,800,000$ virtual seismic stations with a spacing of ~ 500 m. The vertical components exhibit particularly high spatial variability in the inferred f_c .

We find that the directivity effects associated with the bilateral rupture lead to an elevated f_c at both ends of the main fault in the radial and vertical components (Fig. 4a,c and red dashed lines in Fig. 5d). The corner frequency variability of the transverse component (Fig. 4b) is smaller than that of the other components and resembles to first-order a strike-slip radiation pattern: f_c is higher close to the nodal planes and lower where the wavefield amplitudes are expected to be the largest.

A gap between two high- f_c rays in the vertical components (orange lines in Fig. 5d) is related to a major rupture complexity of the mainshock, the “tunneling” dynamics at the intersection with the orthogonal fault F2 (Fig. 3c). We compare the modeled acceleration waveforms at synthetic stations located

within the elevated- f_c regions (stations R1 and R3) with a station located in the gap between the high- f_c rays (station R2) in Figure 5a–c. The waveforms show that regions with high- f_c values are associated with a high-frequency acceleration pulse that is absent in the R2 accelerogram.

Figure 5e,f shows the corresponding peak dip-slip isochrones at high- f_c stations R1 and R3, which we use to identify the origin of the acceleration pulses. The acceleration pulse at R1 occurs shortly after 17 s simulation time. This 17 s pulse originates from an “isochrone jump” at the intersection with the orthogonal fault F2 close to the surface. This isochrone jump is caused by the abrupt stopping of the rupture at the intersection at shallow depth and delayed activation of the fault area behind the intersection. The complex shape of the peak dip-slip isochrones in the shallow area before the fault intersection (Fig. 5e) is caused by a secondary surface-reflected rupture front, which involves a pronounced rake rotation (Fig. 2b). The complex dynamics of surface rupture, rake rotation, and abrupt rupture arrest at the geometric barrier formed by the fault intersection conjointly generate pronounced high-frequency radiation in the vertical component. The high- f_c ray, in which R1 is located (Fig. 5d), reflects a high-amplitude lobe in the rupture-forward direction of a P–SV radiation pattern of this high-frequency dynamics.

The same mechanism of surface dynamic rupture, rake rotation, and arrest explains the high acceleration pulse recorded at R3. This pulse occurs at 20 s, which coincides with the surface-breaking and rake-rotated rupture front stopping abruptly at the southern end of the fault system. Its amplitude is higher because this station is closer to the fault, the directivity effect is stronger, and rupture deceleration may appear as more abrupt. The isochrones show the first upgoing rupture front, whereas the vertical acceleration pulses are associated with the deceleration of the surface-reflected rupture front. This leads to a timing discrepancy of ~ 1 s between the high-frequency pulse in the accelerogram and the rupture stopping indicated by the isochrones.

The spectra of the observed near-field vertical ground motions show similar spatial variability in f_c as the dynamic rupture model of the 2019 Ridgecrest mainshock. In Figure 5d, we show the vertical f_c values of the observed spectra at 17 near-field stations (Fig. S5). The observed f_c values depend on azimuth and mostly resemble the synthetic f_c map. Six stations are located in rupture forward direction at the northern end of the fault system, and f_c values at four of these stations agree with our modeled values, whereas f_c at two stations is lower than in our model. We may speculate that a slightly different location of rupture arrest to the north or unmodeled site effects cause this discrepancy. The station with the highest observed f_c is located at the southern end of the fault system where the strongest directivity is expected, which agrees with our model. Figure S5 shows that the synthetic spectra generally reproduce the observed spectra. The

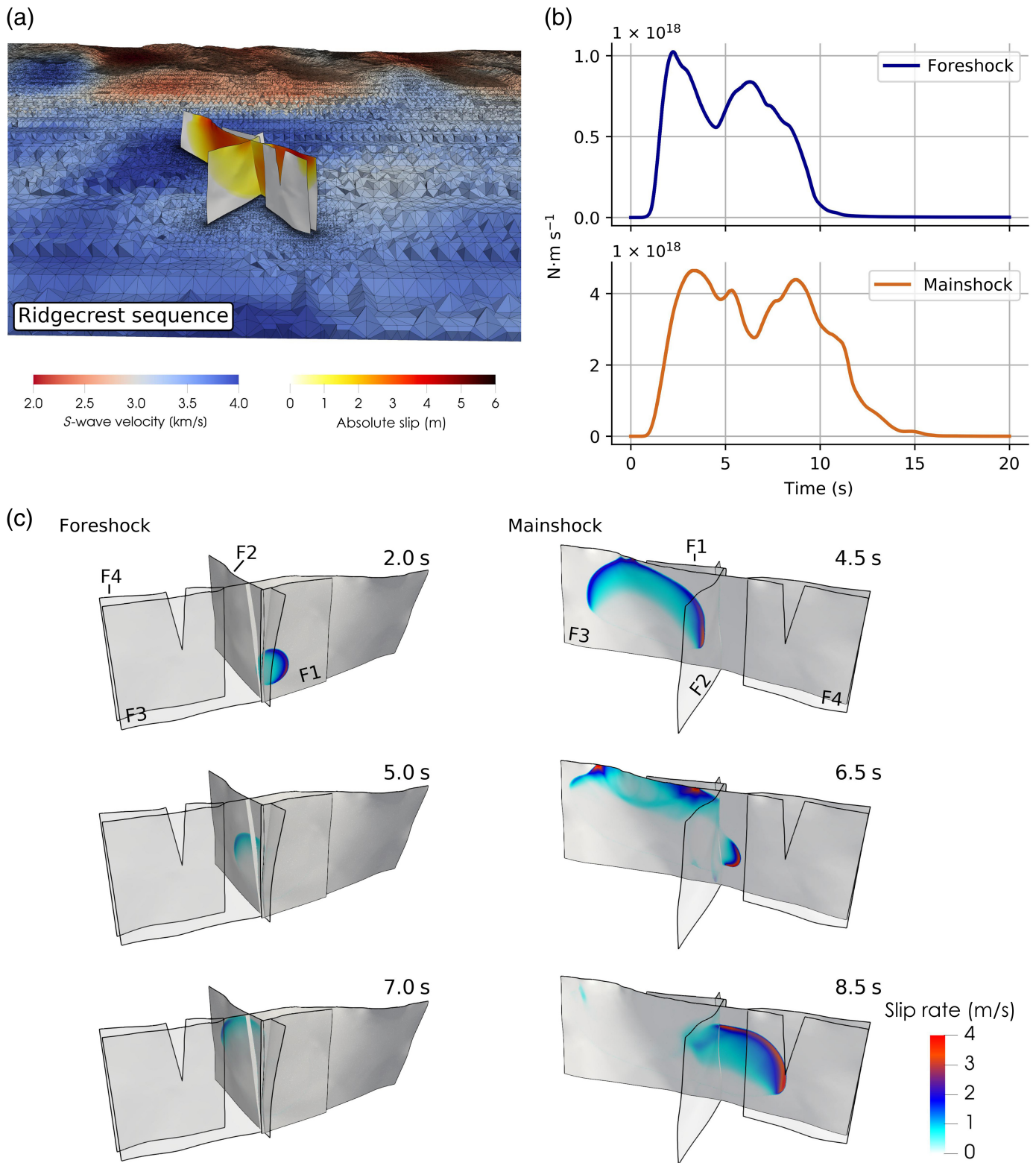
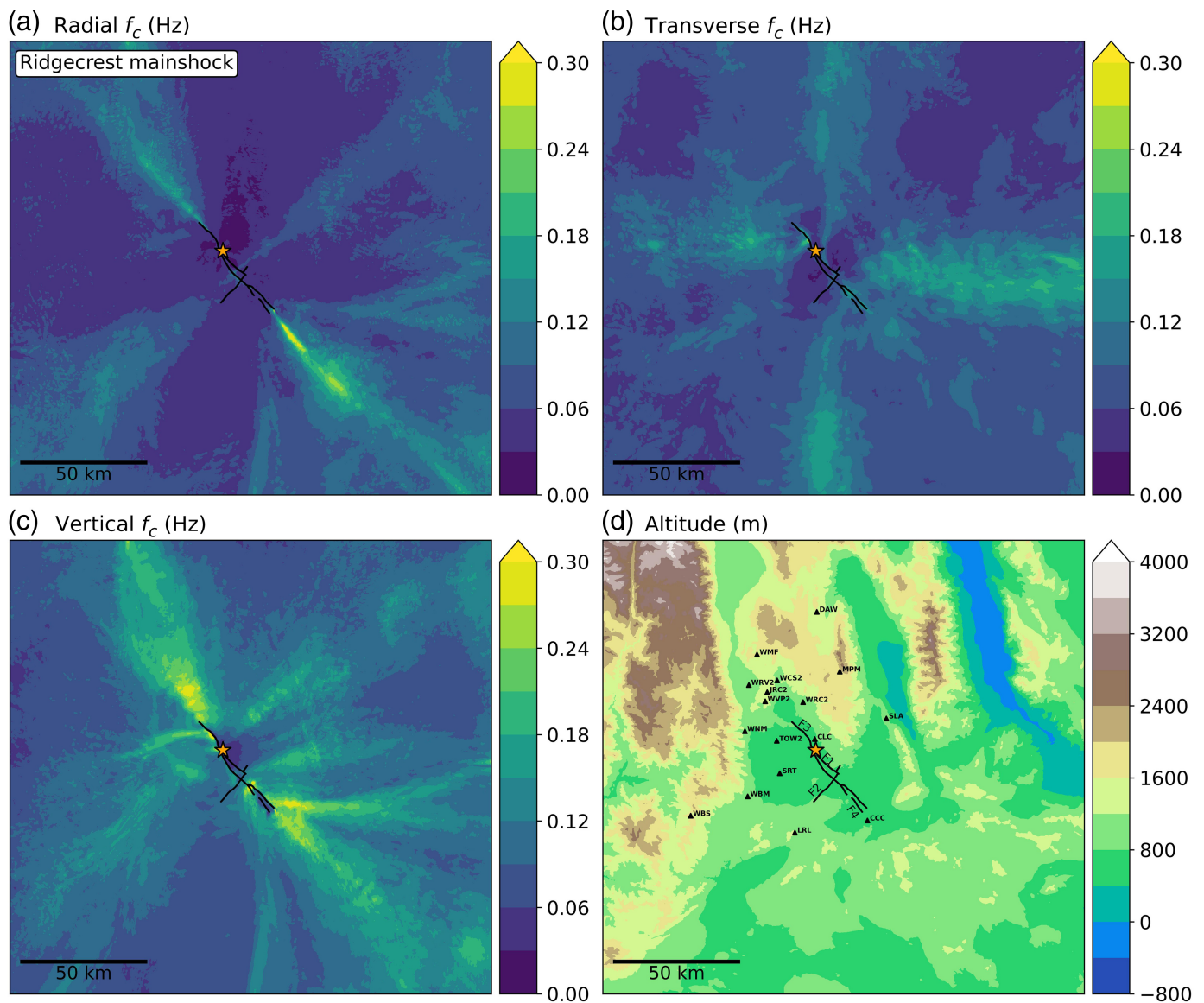


Figure 3. Overview of the 2019 Ridgecrest sequence (linked M_w 6.4 Searles Valley foreshock and M_w 7.1 Ridgecrest mainshock) 3D dynamic rupture models adapted from [Taufiqurrahman et al. \(2023\)](#). (a) Fault geometry with slip distribution after both earthquakes and crosscut of the unstructured tetrahedral computational mesh colored by the used 3D variable S-wave velocity (CVM-S4.26; [Lee et al., 2014](#)). (b) Seismic

moment release rate for both foreshock and mainshock. (c) Slip rate snapshots across the orthogonal fault system at selected rupture times, illustrating dynamic rupture evolution and complexity. The foreshock dynamic rupture scenario is shown on the left side, and the mainshock is on the right side. The color version of this figure is available only in the electronic edition.



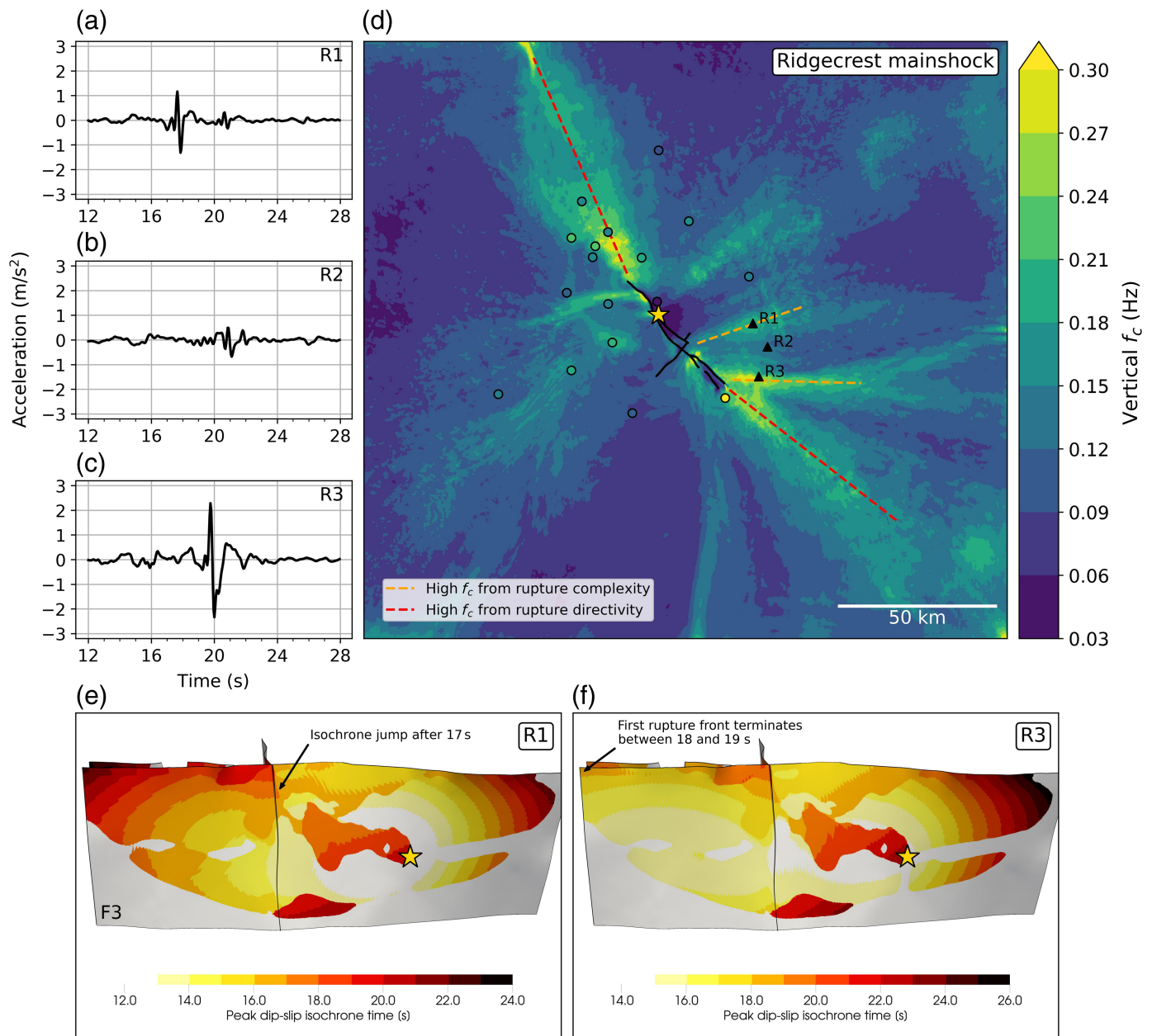
observed spectra fit the Brune model to first order; however, local deviations in limited frequency bands also occur.

The dynamic rupture model of the Searles Valley foreshock initiates close to the F1–F2 fault intersection (Fig. 3c). Right-lateral slip on F1 spontaneously ceases without reaching the surface, which agrees with observations (Liu *et al.*, 2019). The deep rupture on F1 activates the conjugate, critically prestressed left-lateral fault F2. F2 ruptures entirely to its southwestern end, accumulating most of the event's slip and breaking the surface over its full length.

Although both events, the mainshock, and the foreshock, are rupturing the same fault system, their vertical f_c distributions differ vastly. This illustrates that f_c is dominated by source effects. In Figure 6d we observe a wide f_c -shadow zone, an area of smaller than average f_c , in the rupture backward-directivity direction (northeast), which reflects the dominantly unilateral nature of the foreshock rupture. A thin ray of elevated f_c within this shadow zone emits from the small

Figure 4. Map view of the Ridgecrest mainshock's equivalent near-field corner frequency (f_c) distribution of the (a) radial, (b) transverse, and (c) vertical components of synthetic seismograms simulated at $\sim 1,800,000$ virtual seismic stations. The synthetic seismograms are generated from the complex 3D dynamic rupture model of the 2019 Ridgecrest mainshock (Fig. 3). (d) Map view of the model's topography. The black lines indicate the numbered fault traces, triangles show near-field station locations, and the star marks the epicenter. The color version of this figure is available only in the electronic edition.

nonsurface rupturing slip patch at the northwest-trending F1 (Fig. 3c). Our results show high- f_c structures (highlighted with dashed orange lines in Fig. 6d) pointing away from the southwestern part of the primary fault F2, where the rupture breaks the surface. A gap in these high- f_c rays coincides with a small kink of the fault trace.

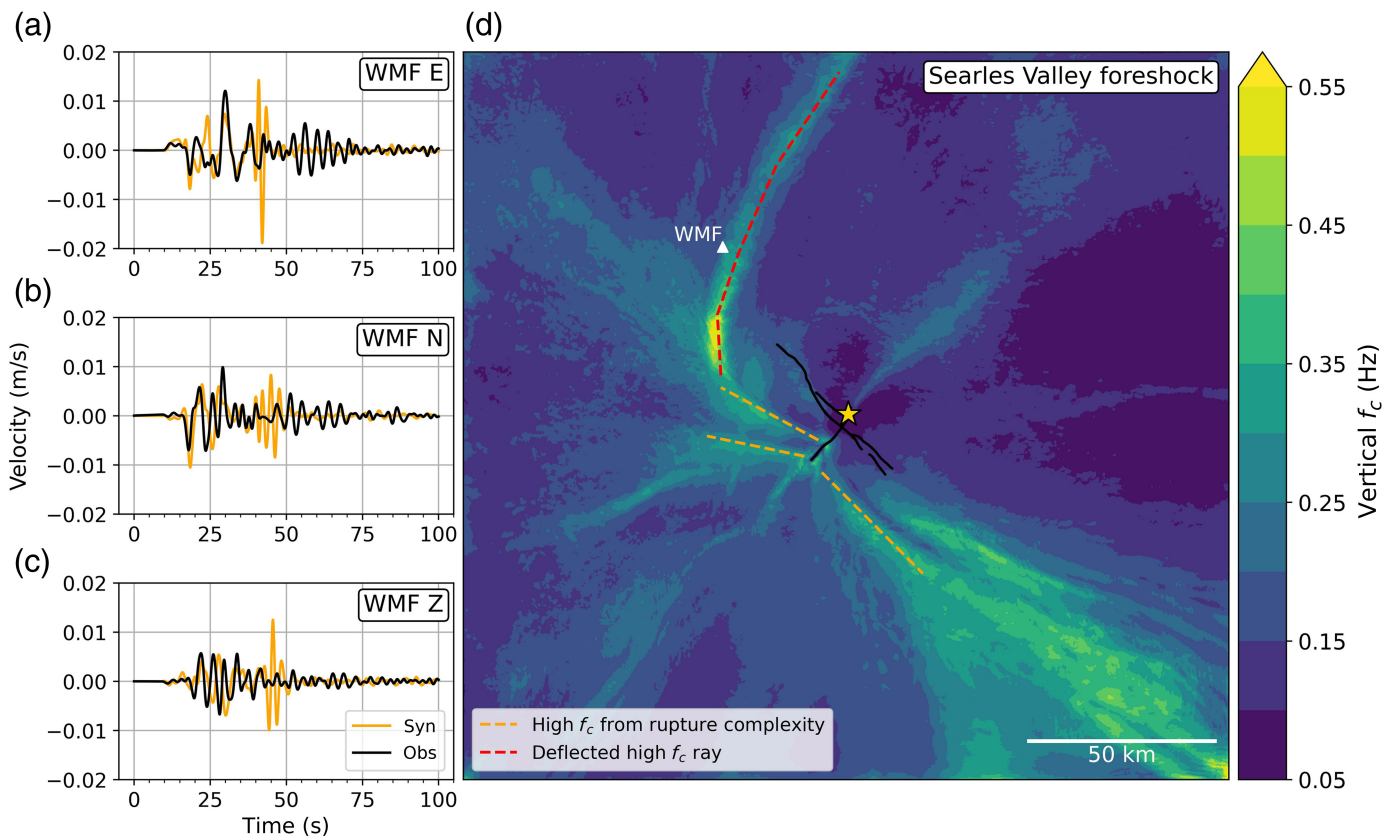


A pronounced feature in the vertical f_c distribution of the Searles Valley foreshock is a curved-path high- f_c ray (dashed red line in Fig. 6d), which changes direction from west-northwest to northeast. Its bent structure is caused by deflection at the strong velocity contrast along the southern Sierra Nevada mountain range (Fig. 4d). An animation of the 3D wavefield (see [Data and Resources](#)) illustrates these locally strong path effects.

Seismic energy is directed in unexpected directions and significantly prolongs the observed shaking duration at several stations, for example, at station WMF. Figure 6a–c shows synthetic and observed waveforms at station WMF, which are low-pass filtered at 0.5 Hz. In this frequency range, the synthetic ground motions of the directly arriving wave packet agree well with the observations (before 40 s). For the second wave packet, which is associated with the deflection at the

Figure 5. (a,b,c) Ridgecrest mainshock's synthetic vertical ground accelerations at three selected stations. (d) Map view of the equivalent near-field corner frequency (f_c) distribution of the vertical components of synthetic seismograms recorded at $\sim 1,800,000$ virtual seismic stations. The synthetic seismograms are generated from a complex dynamic rupture model of the 2019 Ridgecrest mainshock (Fig. 3). The black lines indicate the fault traces, the star marks the epicenter, colored dots show f_c values of recorded ground motion spectra, and triangles show the virtual station locations of the analyzed accelerograms. The orange and red lines mark different high- f_c features. (e,f) Peak dip-slip isochrones of stations R1 and R3. The color version of this figure is available only in the electronic edition.

mountain range, there are significant differences between the synthetic and observed waveforms. The synthetic wave packet arrives earlier, has a shorter duration, and contains



single high-frequency spikes in the EW and Z components. These differences may be explained by a lack of small-scale subsurface heterogeneity in the 3D velocity model used in the dynamic rupture simulation. Additional high-frequency wave scattering may prolong coda-shaking (e.g., [Imperator and Mai, 2012](#); [Takemura et al., 2015](#); [Taufiqurrahman et al., 2022](#)). The travel-time difference may be caused by underestimating the velocity reduction of a sedimentary basin between the mountain range and the fault system in the used 3D velocity model (CVM-S4.26; [Lee et al., 2014](#)). To not omit late-arriving deflected waves, we derive f_c values in Figure 6d from the full-time series of the simulation (100 s duration after the nucleation) without picking a body-wave window. The same plot with selecting a body-wave window is shown in Figure S2. The body-wave window removes the curved high- f_c ray, but otherwise, the f_c distribution is nearly identical.

1992 Landers earthquake

The dynamic rupture model of the 1992 Landers earthquake by [Wollherr et al. \(2019\)](#) ruptures across five fault segments (Fig. 7, and for an animation see [Data and Resources](#)). Rupture nucleates at the southern part of the Johnson Valley fault (JVF) and propagates northward. After 4 s, the rupture migrates to the Kickapoo fault (KF) by direct branching. The Kickapoo fault connects the rupture from the JVF to the Homestead Valley fault (HVF). The rupture nearly stops at a fault bend at the HVF but then reinitiates

Figure 6. Searles Valley foreshock's synthetic and observed velocity seismograms of the (a) east (E), (b) north (N), and (c) up (Z) components at station WMF. In difference to [Taufiqurrahman et al. \(2023\)](#), we here show seismograms not normalized and including higher frequencies, low-pass filtered to 0.5 Hz to highlight the match of the first wave packet. (d) Map view of the equivalent near-field corner frequency (f_c) distribution of the vertical components of synthetic seismograms simulated at $\sim 1,800,000$ virtual seismic stations (without picking a body-wave window). The seismograms are generated from the complex 3D dynamic rupture model of the 2019 Searles Valley foreshock (Fig. 3). The black lines indicate the fault traces, the star marks the epicenter, and the triangle shows the location of the station WMF. The color version of this figure is available only in the electronic edition.

and breaks up to its northern extent. Although rupturing the HVF, a second rupture front branches to the Emmerson fault (EF). At around 15.5 s, a part of the EF is also activated by dynamic triggering from waves generated at the northern part of the HVF. Multiple rupture fronts (including backpropagating rupture fronts) form when the slower rupture front from direct branching reaches the part of the EF that was dynamically triggered. The backward propagating rupture dynamically reactivates parts of the HVF and the KF. After 22.3 s, a completely separate subevent on the Camp Rock fault (CRF) is dynamically triggered by the superimposed waves generated at the EF and the northern part of the HVF. The rupture completely stops after 30 s.

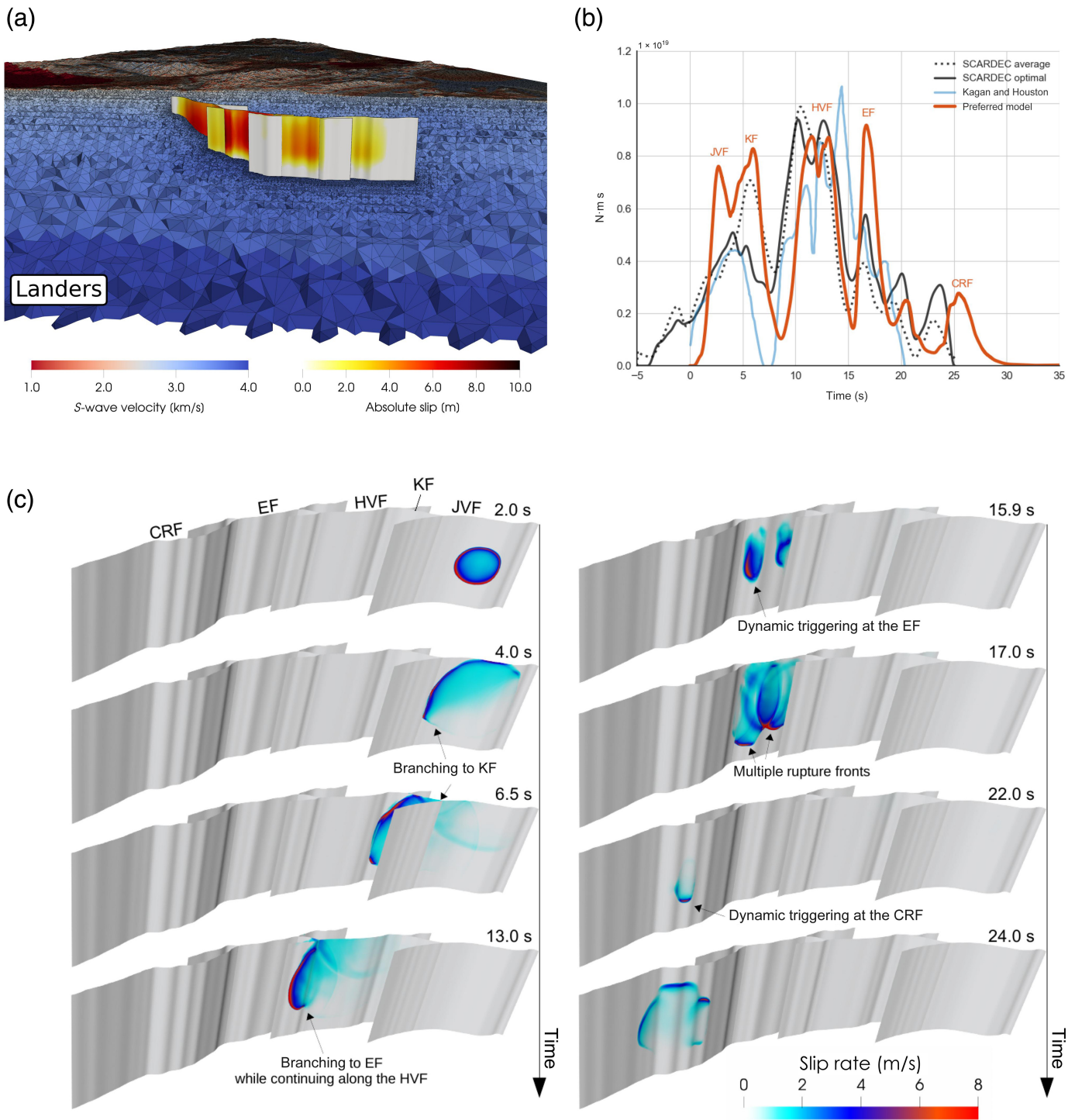


Figure 7. Overview of the 1992 Landers earthquake 3D dynamic rupture model adapted from [Wollherr et al. \(2019\)](#). (a) Fault geometry with accumulated slip distribution and crosscut through the unstructured tetrahedral computational mesh colored by the used 3D variable S -wave velocity ([Shaw et al., 2015](#)). (b) Seismic moment rate release rate. The Landers dynamic rupture model (preferred model, orange) is compared to the optimal and average moment rate release of the SCARDEC database (in black and dotted light gray, [Vallée and Douet, 2016](#)) and the inferred

moment rate based on the surface slip (in light blue, [Kagan and Houston, 2005](#)). CRF, Camp Rock fault; EF, Emerson fault; HVF, Homestead Valley fault; KF, Kickapoo fault; JVF, Johnson Valley fault. (c) Slip rate snapshots across the fault system at selected rupture times illustrating dynamic rupture evolution and complexity. Rupture cascades across fault segments through direct branching and dynamic triggering. The color version of this figure is available only in the electronic edition.

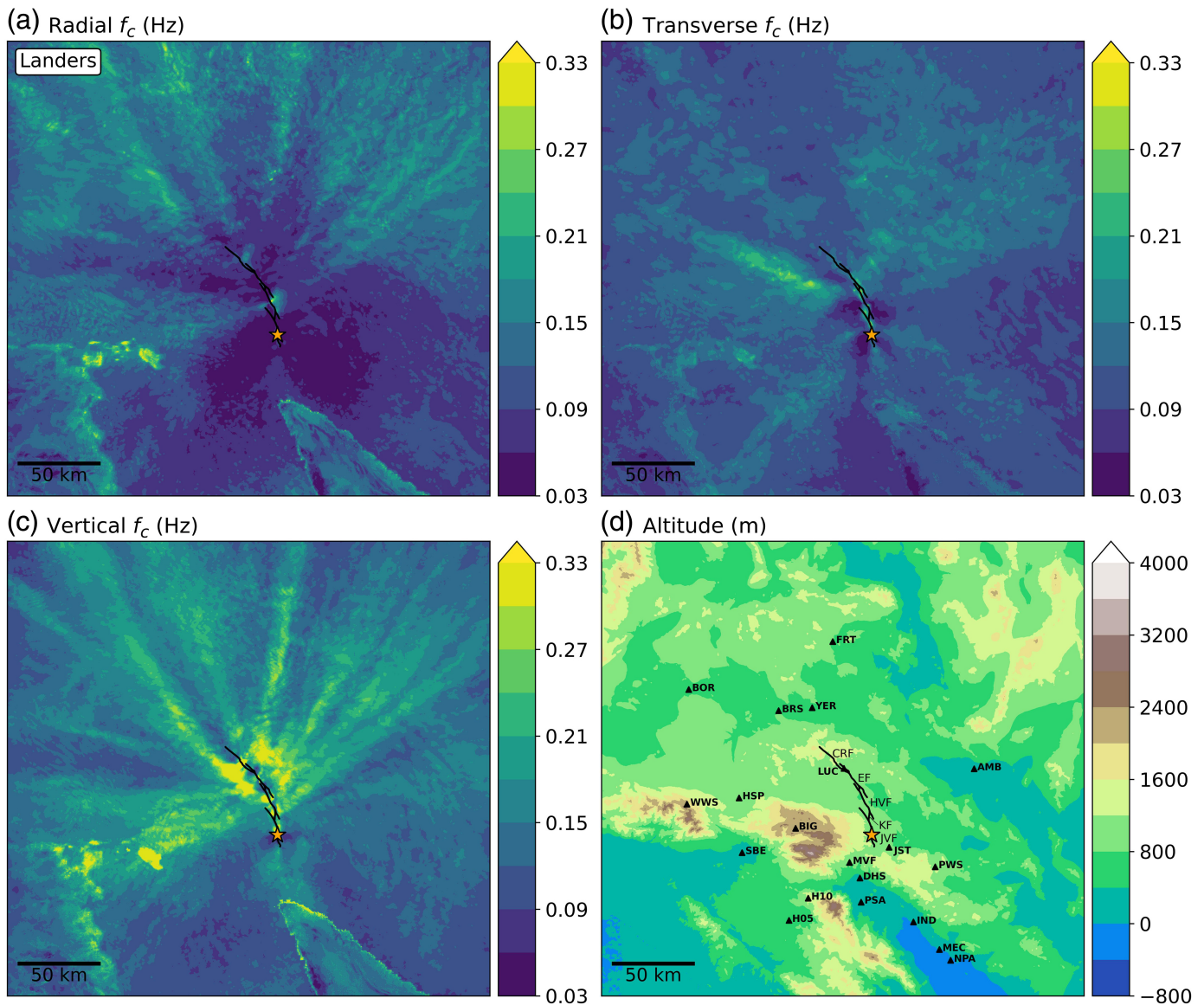
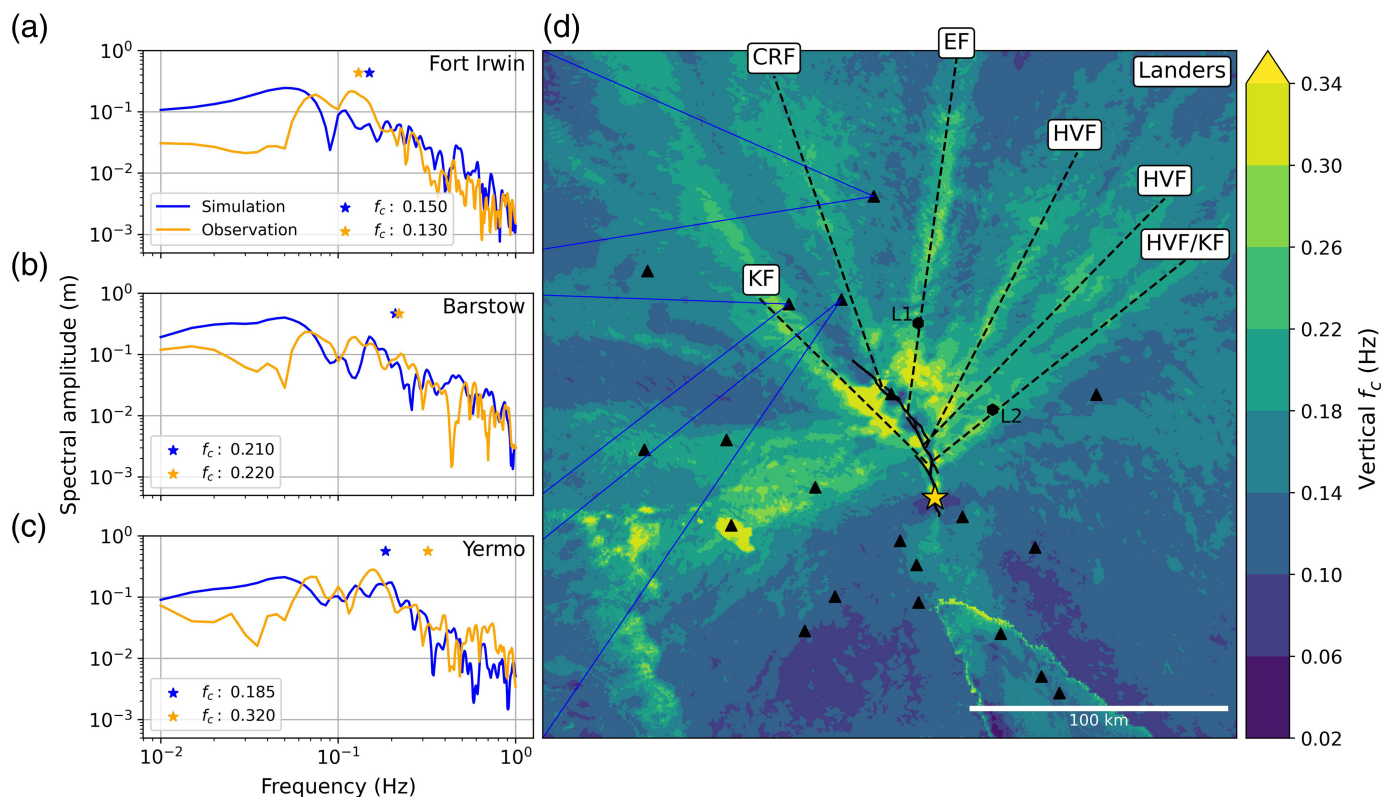


Figure 8a–c shows the equivalent near-field corner frequency f_c distributions of the Landers dynamic rupture simulation computed at $\sim 1,000,000$ virtual seismic stations. The vertical components, as well as parts of the radial components, exhibit considerable spatial variability in the inferred f_c , whereas the spatial variability of f_c of the transverse components is lower. The vertical component shows a complex pattern of localized rays of increased f_c , pointing away from the fault trace. We observe a correlation between the distribution of f_c in the vertical and radial components, which we interpret as an indication that the P – SV wave modes are responsible for the observed rays.

Sharp changes of f_c outline several low-velocity sedimentary basins, such as the Salton Sea basin in the South and the San Bernardino and Los Angeles basins in the southwest. Low-velocity sediment basins lead to sharp corner frequency increases of the P – SV mode at their edges. Although this is a plausible mechanism, we here clip the color map at

Figure 8. Map view of the Landers earthquake's equivalent near-field corner frequency (f_c) distribution of the (a) radial, (b) transverse, and (c) vertical components of synthetic seismograms simulated at $\sim 1,000,000$ virtual seismic stations. The seismograms are generated from the complex 3D dynamic rupture model of the 1992 Landers earthquake (Fig. 7). We clip the color map at sedimentary basins and close to the fault, where static displacement and an inaccurate component separation due to finite-fault effects distort the corner frequency determination. We omit these regions in our interpretation. (d) Map view of the model's topography. The black lines indicate the fault traces, triangles show station locations, and the star marks the epicenter (CRF, Camp Rock fault; EF, Emerson fault; HVF, Homestead Valley fault; JVF, Johnson Valley fault; KF, Kickapoo fault). The color version of this figure is available only in the electronic edition.

sedimentary basins and close to the fault, where static displacement and an inaccurate component separation due to finite-fault effects distort the corner frequency determination, and we omit these regions in our interpretation.



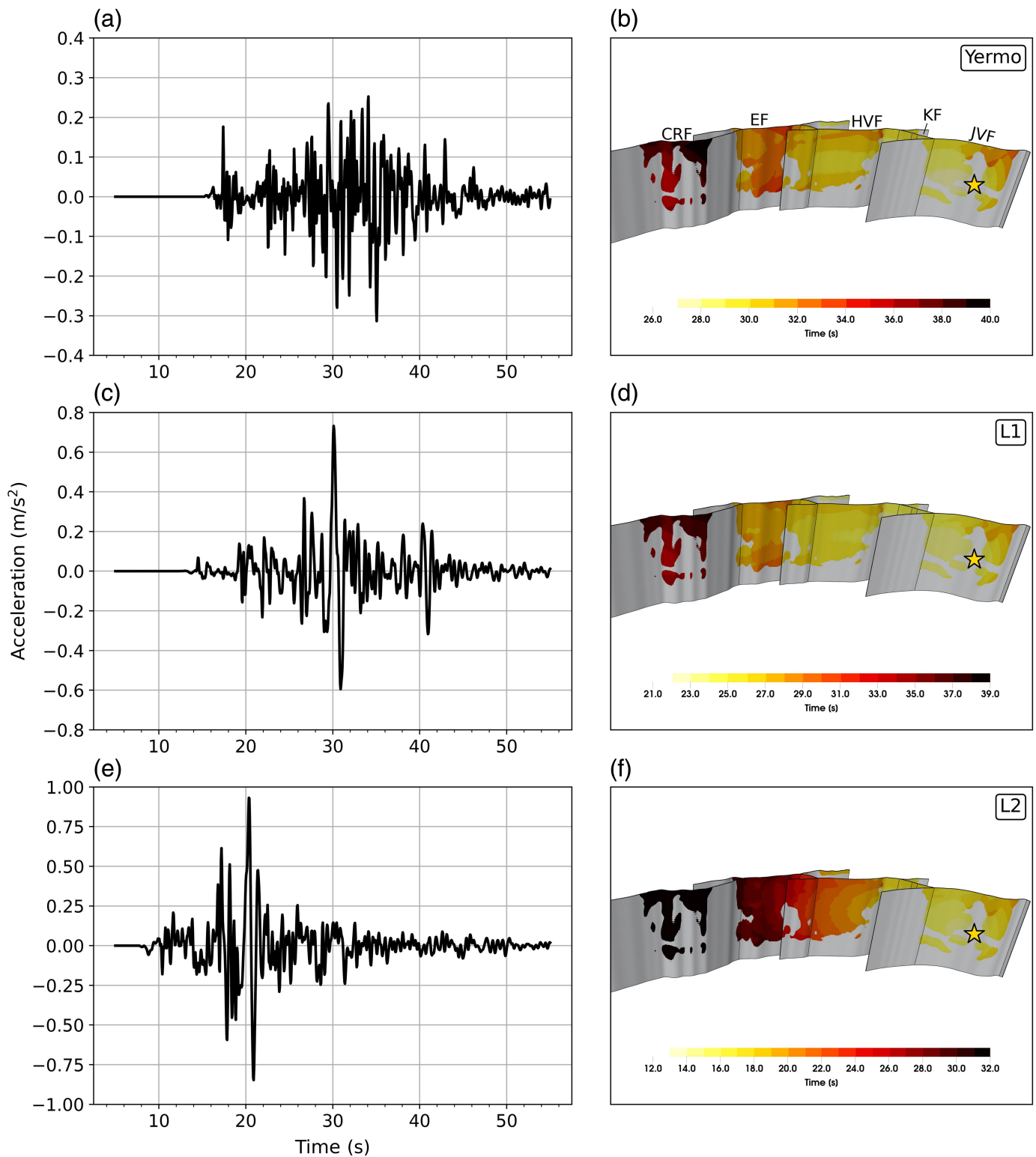
We highlight the rays of high f_c in the vertical components of the Landers model as dashed lines in Figure 9d. These rays mostly takeoff at an angle close to 45° to the rupture forward direction, and they trace the curvature of the segmented fault system. South of the epicenter, f_c is generally lower, although this is overprinted by a local increase due to the Salton Sea basin. Decreased southern f_c is caused by the directivity effects of the north-northwestward-directed unilateral rupture, which prolongs shaking in the backward direction and mitigates the high-frequency content. We note that analyzing the vertical components of the Landers model can lead to a higher average f_c because it consists of more sharply separated subevents and dip-slip patches (Fig. 7; Das and Aki, 1977).

Three seismic stations (Fort Irwin, Barstow, and Yermo), which recorded near-field waveforms of the 1992 Landers event, are located on or between our modeled rays of elevated corner frequencies. Comparing the observed spectra with our synthetic data reveals an excellent fit between 0.1 and 1.0 Hz (Fig. 9a–c). Station Fort Irwin is located between two high- f_c rays and has a lower f_c than the spectra of the stations Barstow and Yermo, which are located on high- f_c rays. Spectra recorded at other near-field stations agree well with the synthetic spectra between 0.1 and 1.0 Hz (Fig. S6).

We use isochrone theory to identify the source of the elevated f_c rays in the vertical components. The rupture process of the Landers model is complicated and often involves multiple rupture fronts and reactivation of slip, whereas the isochrones can capture only a single phase of slip (see the animation of the rupture process, Data and Resources).

Figure 9. Observed spectra and corresponding f_c of the 1992 Landers earthquake compared with synthetic counterparts at three selected stations: (a) Fort Irwin, (b) Barstow, and (c) Yermo. The spectra are not normalized but reflect absolute values. (d) Same as Figure 8c. The black solid lines indicate the fault traces, the star marks the epicenter, triangles are real station locations, and hexagons show two virtual stations that are analyzed in Figure 10. The dashed lines highlight rays of high f_c , and the text windows show the fault names where the rays originate (CRF, Camp Rock fault; EF, Emmerston fault; HVF, Homestead Valley fault; KF, Kickapoo fault). We clip the color map at sedimentary basins and close to the fault, where static displacement and an inaccurate component separation due to finite-fault effects distort the corner frequency determination. We omit these regions in our interpretation. The color version of this figure is available only in the electronic edition.

Figure 10a,c,e shows the synthetic ground accelerations at three selected stations: Yermo and two virtual stations L1 and L2 (Fig. 9d). As expected from previous observational analysis (Campbell and Bozorgnia, 1994), directivity effects strongly affect waveforms recorded at Yermo, which is located in the average strike direction of the unilateral rupture. Therefore, Yermo's waveforms overall have a considerable amount of high-frequency shaking and do not exhibit a single spike that is solely responsible for the high f_c . However, we observe that a dynamically triggered subevent at the Camp Rock fault causes the highest waveform amplitudes at about 36 s (Fig. 10a,b). This subevent initiates at 8 km depth, breaks the surface, and terminates during a short period of time,



which superimposes the overall source spectrum with a source spectrum of a lower magnitude subevent corresponding to a higher f_c . The same subevent causes a strong signal at about 40 s at L1.

The accelerogram at virtual station L1 is dominated by a pulse starting at about 29 s. The isochrones show that the source of the high-frequency radiation recorded at L1 is located

Figure 10. (a,c,e) Landers earthquake's synthetic vertical accelerograms at three selected stations: Yermo, L1, and L2 (Fig. 9d). (b,d,f) Peak dip-slip isochrones of the respective stations. The star marks the hypocenter (CRF, Camp Rock fault; EF, Emmerson fault; HVF, Homestead Valley fault; JVF, Johnson Valley fault; KF, Kickapoo fault). The color version of this figure is available only in the electronic edition.

either at the top or at the bottom of the rupture zone of the EF. The animation of the rupture shows that a dynamically activated backpropagating rupture front coalesces with a forward-propagating rupture front, which causes high-amplitude up-dip and down-dip propagating rupture fronts (Fig. S3c,d). The down-dip propagating front arrests when it reaches the bottom of the seismogenic zone, and the up-dip propagating front breaks the surface until it stops abruptly at the kink to the CRF. This shallow surface-breaking rupture is dominant in generating the vertical acceleration pulse at L1 because it involves an average rake rotation of up to 10° (Fig. 2c), which is not observed at the bottom of the rupture zone.

The accelerogram of the virtual station L2 contains two strong high-frequency pulses, the first starting at about 16 s and the second starting at 19 s. The isochrones show that the first high-frequency pulse coincides with the surface rupture at the kink between the JVF and the KF; therefore, the source might be a so-called kink wave (Adda-Bedia and Madariaga, 2008) from the rake-rotated rupture front propagating along the surface. However, another rupture front propagates up-dip along the kink simultaneously (Fig. S3a). This coalescence of differently directed rupture fronts likely also contributes to the modeled high-frequency radiation. A similar mechanism, a coalescence of an up-dip propagating rupture front and an along-strike propagating rupture front at the fault kink between the KF and the HVF segments generates the second high-frequency pulse (Fig. S3b). There is a small discrepancy between the isochrone timing and the high-amplitude spike in the waveforms because the isochrones capture the rupture front that propagates up-dip along the kink, whereas the along-strike propagating rupture front arrives later but still interacts with the former. We observe large and localized shallow rake rotation at both kinks (Fig. 2c).

Discussion

In our analysis of four dynamic rupture scenarios of large strike-slip earthquakes with varying source complexity, we find localized rays of elevated f_c in the vertical components of each event. Albeit path and 3D basin effects, this variability in equivalent near-field corner frequencies is dominated by source effects. The large vertical high-frequency radiation is caused by complex dynamic mechanisms, including shallow dip-slip generated by a rake rotation when the rupture breaks the surface and strong stopping phases due to rupture complexity, for example, at a barrier or a fault kink. The high-amplitude lobes of the P - SV radiation pattern and the directivity effect shape the rays to form a 45° angle to the rupture forward direction.

Our results imply that high- f_c rays correlate with certain characteristic rupture dynamics. The rays often point to locations where dynamic rupture decelerates suddenly, specifically during the breaking of the Earth's surface. Abrupt stopping is usually caused by rupture complexity. For example, dynamic rupture decelerates quickly when tunneling underneath an

orthogonal intersecting fault in the simulations of the 2019 Ridgecrest sequence. Other rupture complexities that can cause localized high-frequency radiation are fault kinks or sudden changes in along-strike fault geometry, as we observe in the dynamic rupture model of the 1992 Landers earthquake at the JVF-KF and the KF-HVF fault intersections. Our findings can provide a physical explanation of observations that fault "misalignment" (Chu *et al.*, 2021) correlates with enhanced high-frequency seismic radiation due to a typically higher degree of geometric complexity, including more intersecting faults and fault kinks.

Near-field corner frequency analysis may help to constrain slip distribution and slip segmentation at depth. Such analysis can also help correlate fault segments with respective subevents in the moment rate release function of large earthquakes. We find that high- f_c rays can indicate locations of surface rupture. Deconvolution of the observed regional ground motions at a station located perpendicular to the rupture direction of the 1992 Landers earthquake shows that surface offsets correlate with the on-fault slip distribution and structural complexity (e.g., Kanamori *et al.*, 1992; Milliner *et al.*, 2015). The moment rate function of the Landers dynamic rupture model shows that it consists of four sharply separated subevents (Fig. 7b, Kagan and Houston, 2005; Vallée and Douet, 2016). Each of these high- f_c rays that we identify can be clearly associated with one of these subevents. Even the weak moment rate subevent corresponding to the Camp Rock fault rupture is clearly detectable in the f_c distribution. Because this rupture on the Camp Rock fault is dynamically triggered in our dynamic rupture scenario and spatially separated from the other slipping parts of the fault system, its associated spectral contribution includes complete nucleation and stopping phases and superimposes the overall source spectrum with a secondary spectrum with a higher f_c .

Although our results show that source complexity strongly affects f_c in the near field, the impact of source complexity on far-field corner frequencies, and, thus, Brune-type stress-drop estimates, may also be larger than typically assumed from simpler rupture models (e.g., Madariaga, 1976, Kaneko and Shearer, 2015; Wang and Day, 2017). Circular and elliptical rupture models show a significant azimuthal f_c variation caused by rupture directivity and nodal plane effects. Figures S7 and S8 show a comparable effect of directivity on the azimuthal f_c distribution in our Ridgecrest mainshock and Landers earthquake models. However, in addition, directivity effects are overprinted by small-scale complexity. As a result, the relative variability of f_c values is $\sim 35\%$ smaller compared with the simpler models of Kaneko and Shearer (2014). The standard deviation of f_c in our models strongly depends on the azimuth and is generally higher in the vertical components.

Liu *et al.* (2023) found that Brune-type corner frequencies of the spectra of the source time functions of complex events correlate best with the corner frequency of that subevent with

the highest moment release. They conclude that the Brune stress drop reflects the stress change of the largest asperity. Our observed spatial variability of f_c in dynamic rupture simulations paints an even more complex picture, identifying dynamic earthquake characteristics as an important source of ground-motion spectra variability. Recent observations align with our findings: [Calderoni and Abercrombie \(2023\)](#) compare stress drops inferred from finite-fault modeling with Brune-type corner frequencies for the M_w 6.0 Amatrice and the M_w 5.9 Visso events in Italy. They find that high spectral corner frequencies may not be directly associated with high stress drops but rather reflect high-frequency ground motions caused by rupture complexity. [Gallovič and Valentová \(2020\)](#) compare stress-drop estimates inferred from f_c of the modeled moment rate functions with the on-fault measured value for ~1600 strike-slip dynamic rupture models. They find that f_c is affected by details of the generally heterogeneous rupture propagation that cannot be attributed to a single stress-drop parameter. Our results highlight the importance of good azimuthal coverage when inferring Brune-type stress drops from corner frequencies (e.g., [Kaneko and Shearer, 2015](#)). Future larger-scale dynamic rupture simulations may investigate dynamic source effects also on far-field stress drops. The presented dynamic rupture scenarios lack small-scale dynamic rupture heterogeneity ([Taufiqurrahman et al., 2022](#); [Gallovič and Valentová, 2023](#)), which is associated with a depletion of high-frequency content. However, we expect that including smaller scale rupture complexity may not imprint on the frequency ranges that are most relevant for computing f_c in our dynamic rupture models of relatively large earthquakes. Analyzing much smaller magnitude events is possible but would require a finer model discretization (i.e., a higher computational cost) to sufficiently resolve the higher frequency bands, for example, associated with a higher f_c .

It will be interesting to further investigate the effects of different 3D velocity models and their uncertainties, particularly in the near-source region. For example, fault damage zones may affect ground motions over large distances and amplify high-frequency radiation in certain directions ([Huang et al., 2016](#); [Yeh and Olsen, 2023](#)).

We believe that our results are generally representative of surface-breaking multifault strike-slip events (e.g., [Jia et al., 2023](#)). However, it will be more challenging to apply our approach to analyze reverse or normal-faulting events. There, the component separation is more difficult, and the free surface has an asymmetric effect (e.g., [Oglesby et al., 1998, 2000](#); [Biemiller et al., 2022](#)). Similarly interesting and challenging would be applying our approach to mixed-faulting multifault events such as the 2016 M_w 7.8 Kaikōura earthquake ([Ulrich, Gabriel, et al., 2019](#)).

[Umeda \(1990\)](#) introduced the concept of an “earthquake bright spot” as a localized area in the shallow fault region that emits strong high-frequency waves. Specifically, the Landers earthquake fault system kink where the JVF branches into

the KF has been identified as an earthquake bright spot ([Yamashita and Umeda, 1994](#)), which agrees with our dynamic rupture model analysis, in which it is a prominent source of a ray of elevated f_c . [Yamashita and Umeda \(1994\)](#) propose that the nucleation and arrest of slip on subsidiary faults cause earthquake bright spots. We find that rake-rotated along-strike surface-breaking rupture fronts that encounter geometric fault complexities can locally cause strong acceleration pulses, which can equally explain the origin of earthquake bright spots without the need for secondary faults.

In addition, tossed-up boulders indicate that coseismic vertical accelerations exceeded gravity during the 1992 Landers earthquake ([Yamashita and Umeda, 1994](#)) and similar high vertical accelerations were recorded or inferred for other large strike-slip earthquakes (e.g., [Archuleta, 1982](#); [Strasser and Bommer, 2009](#); [Kaiser et al., 2017](#); [Hough et al., 2020](#)). Numerous vertical acceleration recordings of reverse-faulting earthquakes exceeded gravity (e.g., [Bilham and England, 2001](#); [Causse et al., 2021](#)), which is not unexpected because the vertical components are affected more strongly by *SH* waves. We demonstrate how complex source mechanisms of surface-rupturing strike-slip events can cause strong vertical acceleration pulses that may locally exceed gravity.

Equivalent near-field corner frequency analysis of the M_w 6.4 Searles Valley model showcases the capability of f_c variability to track major path effects. A mountain range deflects a high-frequency wave packet and directs seismic energy in an unexpected direction. We find evidence of this deflection in observed waveforms, for example, at station WMF (Fig. 6a–c), where this effect doubles the shaking duration. Such path effects can be relevant for seismic hazard assessment but may be missed in ground-motion models that do not include variability in shaking duration.

Although each presented f_c distribution map is inferred from more than 1,000,000 virtual stations, important aspects of our findings are equally inferable from lower resolution analysis, for example, using only 1% of the data (~10,000 virtual stations with a spacing of ~5 km, Fig. S4), which is promising for potential real-world applicability of the method. For example, the six high- f_c rays pointing away from the fault trace and the sharp f_c increase at the Salton Sea basin in the south and the San Bernardino and Los Angeles basins in the southwest, are still clearly visible in the low-resolution version of the vertical f_c distribution of the Landers model (Fig. S4). Similarly dense seismic sensor networks are becoming feasible and allow the study of seismic source processes with increasing detail. For example, the LARge-*n* Seismic Survey in Oklahoma (LASSO) experiment deployed more than 1800 vertical-component nodal seismometers covering a 25 km by 32 km region with a station spacing of ~400 m ([Dougherty et al., 2019](#)). [Trugman et al. \(2021\)](#) used the LASSO array to investigate the frequency dependence of observed radiation patterns of M_L 1.7–2.8 events and found that a strong isotropic

component at higher frequencies is likely caused by source complexity. DAS can provide linear arrays with a sensor spacing of ~ 10 m (e.g., Zhan, 2019). Li, Kim, *et al.* (2023) used backprojected DAS data to identify high-frequency subevents of the 2021 Antelope Valley earthquake.

Conclusions

In this study, we present a detailed analysis of the spatial variability of an equivalent near-field corner frequency f_c in large strike-slip 3D dynamic rupture simulations. We discover patterns of highly variable f_c and show that f_c variability is dominantly controlled by source effects. Rays of locally increased f_c values radiate outward from the dynamically slipping faults, particularly noticeable in the vertical components. We validate the variability in the distribution of f_c from the dynamic rupture model with those derived from observed spectra. We use isochrone analysis to show that the radiation of vertical high frequencies often results from rake-rotated surface-breaking rupture fronts that decelerate suddenly due to source complexities, such as fault heterogeneities or geometric complexity. We observe that the P - SV radiation pattern, in combination with the directivity effect, shapes high- f_c rays at a 45° angle to the forward rupture propagation direction. This dynamic source effect can potentially explain observations of high-intensity, impulsive near-field vertical ground motions. The analyses of near-field f_c distributions can inform on the characteristics of earthquake kinematics and dynamics including rupture directivity, surface rupture, and fault segmentation. We find that path effects additionally imprint on the dynamic rupture equivalent corner frequencies of near-field spectra. For example, we observe a strong deflection of a high- f_c ray along the southern Sierra Nevada mountain range in the M_w 6.4 Searles Valley simulation. In conclusion, our findings highlight that the equivalent near-field corner frequency may serve as an insightful ground-motion parameter. f_c can be inferred from spatially dense, relatively low-frequency ground-motion data sets, thereby offering an approach to directly infer the spectral fingerprints of rupture dynamics from near-field ground motions. Our study has important implications for seismic hazard assessment and offers new avenues for interpreting large array or DAS data to improve our understanding of the dynamics and ground motions of large earthquakes.

Data and Resources

The described complexity of each dynamic rupture earthquake scenario is best illustrated in animations of the dynamic rupture models of the 1992 M_w 7.3 Landers earthquake available at <https://www.youtube.com/watch?v=zi19g5Jpp5s>, the 2019 M_w 6.4 Searles Valley foreshock available at https://www.youtube.com/watch?v=4b_uhs_rT_g, and the 2019 M_w 7.1 Ridgecrest mainshock available at <https://www.youtube.com/watch?v=8yP0rcC7n-g>. The open-source software package SeisSol is available at <https://github.com/SeisSol/SeisSol>. All input files that are needed to run the Ridgecrest models are available at Zenodo

(<https://zenodo.org/record/6842773>). The SeisSol branch that was used to run the Ridgecrest models is also archived at <https://zenodo.org/record/7642533>. The script that calculates the equivalent near-field corner frequencies from SeisSol's free surface output is provided in the repository available at https://github.com/SeisSol/SeisSol/blob/master/postprocessing/science/spectral_corner_frequency_from_surface_xdmf.py. The script that was used to compute isochrons directly from SeisSol's raw output data are openly available in the SeisSol repository at https://github.com/SeisSol/SeisSol/blob/master/postprocessing/science/compute_isochrones.py. The scripts use the external libraries NumPy and SciPy (Harris *et al.*, 2020; Virtanen *et al.*, 2020). Details about the TPV5 benchmark problem are provided on the homepage of the Southern California Earthquake Center (SCEC)/U.S. Geological Survey (USGS) rupture dynamics code verification community effort available at <https://strike.scec.org/cvws/tpv5docs.html>. All seismic data were downloaded through the Incorporated Research Institutions for Seismology (IRIS) Wilber 3 system available at <https://ds.iris.edu/wilber3/> from the Southern California Seismic Network (CI, California Institute of Technology and U.S. Geological Survey [USGS] Pasadena, 1926). The Python package ObsPy was used to remove the instrument response (Krischer *et al.*, 2015). The other relevant data to Table A1 were available at <https://strike.scec.org/cvws/tpv5docs.html>. The supplemental material contains eight additional figures. All websites were last accessed in November 2023.

Declaration of Competing Interests

The authors acknowledge that there are no conflicts of interest recorded.

Acknowledgments

The authors thank Rachel Abercrombie, an anonymous reviewer, and the Editor-in-Chief Allison Bent for their constructive comments and for handling this article. The authors thank František Gallovič, Jean-Paul Ampuero, and P. Martin Mai for inspiring discussions; and Stephanie Wollherr and Taufiqurrahman for discussing their dynamic rupture models. This study was supported by the European Union's Horizon 2020 Research and Innovation Program (TEAR Grant Number 852992), Horizon Europe (ChEES-2P Grant Number 101093038), DT-GEO (Grant Number 101058129), and Geo-INQUIRE (Grant Number 101058518), the National Aeronautics and Space Administration (Grant Number 80NSSC20K0495), the National Science Foundation (Grant Numbers EAR-2121666 and OAC-2139536) and the Southern California Earthquake Center (SCEC Award Numbers 22135 and 23121). The authors would like to express our gratitude to the Gauss Centre for Supercomputing e.V. available at www.gauss-centre.eu for providing us with computing time on the supercomputer SuperMUC-NG at the Leibniz Supercomputing Centre available at www.lrz.de for our project pr63qo. Additional resources were provided by the Institute of Geophysics of LMU Munich (Oeser *et al.*, 2006).

References

- Abercrombie, R. E. (2021). Resolution and uncertainties in estimates of earthquake stress drop and energy release, *Phil. Trans. Roy. Soc. Lond. A* **379**, no. 2196, doi: [10.1098/rsta.2020.0131](https://doi.org/10.1098/rsta.2020.0131).
- Adda-Bedia, M., and R. Madariaga (2008). Seismic radiation from a Kink on an antiplane fault, *Bull. Seismol. Soc. Am.* **98**, no. 5, 2291–2302.

- Allmann, B. P., and P. M. Shearer (2009). Global variations of stress drop for moderate to large earthquakes, *J. Geophys. Res.* **114**, no. B1, doi: [10.1029/2008JB005821](https://doi.org/10.1029/2008JB005821).
- Andrews, D. J. (1976). Rupture propagation with finite stress in anti-plane strain, *J. Geophys. Res.* **81**, no. 20, 3575–3582.
- Archuleta, R. J. (1982). Analysis of near-source static and dynamic measurements from the 1979 Imperial Valley earthquake, *Bull. Seismol. Soc. Am.* **72**, no. 6A, 1927–1956.
- Arrowsmith, S. J., D. T. Trugman, J. MacCarthy, K. J. Bergen, D. Lumley, and M. B. Magnani (2022). Big data seismology, *Rev. Geophys.* **60**, no. 2, doi: [10.1029/2021RG000769](https://doi.org/10.1029/2021RG000769).
- Ben-Menahem, A. (1962). Radiation of seismic body waves from a finite moving source in the earth, *J. Geophys. Res.* **67**, no. 1, 345–350.
- Bernard, P., and R. Madariaga (1984). A new asymptotic method for the modeling of near-field accelerograms, *Bull. Seismol. Soc. Am.* **74**, no. 2, 539–557.
- Biemiller, J., A.-A. Gabriel, and T. Ulrich (2022). The dynamics of unlikely slip: 3D modeling of low-angle normal fault rupture at the Maï'iu fault, Papua New Guinea, *Geochem. Geophys. Geosys.* **23**, no. 5, doi: [10.1029/2021GC010298](https://doi.org/10.1029/2021GC010298).
- Bilham, R., and P. England (2001). Plateau 'pop-up' in the great 1897 Assam earthquake, *Nature* **410**, no. 6830, 806–809.
- Bizzarri, A. (2010). How to promote earthquake ruptures: Different nucleation strategies in a dynamic model with slip-weakening friction, *Bull. Seismol. Soc. Am.* **100**, no. 3, 923–940.
- Boore, D. M., and W. B. Joyner (1978). The influence of rupture incoherence on seismic directivity, *Bull. Seismol. Soc. Am.* **68**, no. 2, 283–300.
- Breuer, A., A. Heinecke, S. Rettenberger, M. Bader, A.-A. Gabriel, and C. Pelties (2014). Sustained petascale performance of seismic simulations with SeisSol on SuperMUC, in *Proc. of the International Supercomputing Conference*, J. M. Kunkel, T. Ludwig, and H. W. Meuer (Editors) Springer International Publishing, Cham, Germany, 1–18, doi: [10.1007/978-3-319-07518-1_1](https://doi.org/10.1007/978-3-319-07518-1_1).
- Brune, J. N. (1970). Tectonic stress and the spectra of seismic shear waves from earthquakes, *J. Geophys. Res.* **75**, no. 26, 4997–5009.
- Calderoni, G., and R. E. Abercrombie (2023). Investigating spectral estimates of stress drop for small to moderate earthquakes with heterogeneous slip distribution: Examples from the 2016–2017 Amatrice earthquake sequence, *J. Geophys. Res.* **128**, no. 6, doi: [10.1029/2022JB025022](https://doi.org/10.1029/2022JB025022).
- California Institute of Technology and U.S. Geological Survey (USGS) Pasadena (1926). Southern California seismic network, International Federation of Digital Seismograph Networks, doi: [10.7914/SN/CI](https://doi.org/10.7914/SN/CI).
- Campbell, K. W., and Y. Bozorgnia (1994). Empirical analysis of strong ground motion from the 1992 Landers, California, earthquake, *Bull. Seismol. Soc. Am.* **84**, no. 3, 573–588.
- Carena, S., and J. Suppe (2002). Three-dimensional imaging of active structures using earthquake aftershocks: The Northridge thrust, California, *J. Struct. Geol.* **24**, 887–904.
- Causse, M., C. Cornou, E. Maufroy, J.-R. Grasso, L. Baillet, and E. El Haber (2021). Exceptional ground motion during the shallow M_w 4.9 2019 Le Teil earthquake, France, *Commun. Earth Environ.* **2**, no. 1, 14.
- Chu, S. X., V. C. Tsai, D. T. Trugman, and G. Hirth (2021). Fault interactions enhance high-frequency earthquake radiation, *Geophys. Res. Lett.* **48**, no. 20, doi: [10.1029/2021GL095271](https://doi.org/10.1029/2021GL095271).
- Chung, J.-K., and T.-C. Shin (1999). Implication of the rupture process from the displacement distribution of strong ground motions recorded during the 21 September 1999 Chi-Chi, Taiwan earthquake, *Terr. Atmos. Ocean. Sci.* **10**, 777–786.
- Das, S., and K. Aki (1977). Fault plane with barriers: A versatile earthquake model, *J. Geophys. Res.* **82**, no. 36, 5658–5670.
- de la Puente, J., J.-P. Ampuero, and M. Käser (2009). Dynamic rupture modeling on unstructured meshes using a discontinuous Galerkin method, *J. Geophys. Res.* **114**, doi: [10.1029/2008JB006271](https://doi.org/10.1029/2008JB006271).
- Dougherty, S. L., E. S. Cochran, and R. M. Harrington (2019). The LARge-n seismic survey in Oklahoma (LASSO) experiment, *Seismol. Res. Lett.* **90**, no. 5, 2051–2057.
- Dumbser, M., and M. Käser (2006). An arbitrary high-order discontinuous Galerkin method for elastic waves on unstructured meshes II. The three-dimensional isotropic case, *Geophys. J. Int.* **167**, no. 1, 319–336.
- Fan, W., and J. J. McGuire (2018). Investigating microearthquake finite source attributes with IRIS Community Wavefield Demonstration Experiment in Oklahoma, *Geophys. J. Int.* **214**, no. 2, 1072–1087.
- Fleming, R., J. Messerich, and K. Cruikshank (1998). Fractures along a portion of the Emerson fault zone related to the 1992 Landers, California, earthquake: Evidence for the rotation of the Galway-Lake-Road block, *Geol. Soc. Am.* mCH082.
- Galovič, F., and L. Valentová (2020). Earthquake stress drops from dynamic rupture simulations constrained by observed ground motions, *Geophys. Res. Lett.* **47**, no. 4, doi: [10.1029/2019GL085880](https://doi.org/10.1029/2019GL085880).
- Galovič, F., and L. Valentová (2023). Broadband strong ground motion modeling using planar dynamic rupture with fractal parameters, *J. Geophys. Res.* **128**, no. 6, doi: [10.1029/2023JB026506](https://doi.org/10.1029/2023JB026506).
- Graves, R. W., B. T. Aagaard, K. W. Hudnut, L. M. Star, J. P. Stewart, and T. H. Jordan (2008). Broadband simulations for M_w 7.8 southern San Andreas earthquakes: Ground motion sensitivity to rupture speed, *Geophys. Res. Lett.* **35**, no. 22, doi: [10.1029/2008GL035750](https://doi.org/10.1029/2008GL035750).
- Gutteri, M., P. M. Mai, and G. C. Beroza (2004). A pseudo-dynamic approximation to dynamic rupture models for strong ground motion prediction, *Bull. Seismol. Soc. Am.* **94**, no. 6, 2051–2063.
- Harris, C. R., K. J. Millman, S. J. van Waltder, R. Gommers, P. Virtanen, D. Cournapeau, E. Wieser, J. Taylor, S. Berg, N. J. Smith, *et al.* (2020). Array programming with NumPy, *Nature* **585**, 357–362.
- Harris, R. A., M. Barall, B. Aagaard, S. Ma, D. Roten, K. Olsen, B. Duan, D. Liu, B. Luo, K. Bai, *et al.* (2018). A suite of exercises for verifying dynamic earthquake rupture codes, *Seismol. Res. Lett.* **89**, no. 3, 1146–1162.
- Harris, R. A., M. Barall, D. A. Lockner, D. E. Moore, D. A. Ponce, R. W. Graymer, G. Funning, C. A. Morrow, C. Kyriakopoulos, *et al.* (2021). A geology and geodesy based model of dynamic earthquake rupture on the Rodgers Creek-Hayward-Calaveras fault system, California, *J. Geophys. Res.* **126**, no. 3, doi: [10.1029/2020JB020577](https://doi.org/10.1029/2020JB020577).
- Harris, R. A., M. Barall, R. Archuleta, E. Dunham, B. Aagaard, J. P. Ampuero, H. Bhat, V. AtienzaCruz-, L. Dalguer, P. Dawson, *et al.* (2009). The SCEC/USGS dynamic earthquake rupture code verification exercise, *Seismol. Res. Lett.* **80**, no. 1, 119–126.
- Hartzell, S., P. Liu, and C. Mendoza (1996). The 1994 Northridge, California, earthquake: Investigation of rupture velocity, rise time, and high-frequency radiation, *J. Geophys. Res.* **101**, no. B9, 20,091–20,108.

- Haskell, N. A. (1964). Total energy and energy spectral density of elastic wave radiation from propagating faults, *Bull. Seismol. Soc. Am.* **54**, no. 6A, 1811–1841.
- Heinecke, A., A. Breuer, S. Rettenberger, M. Bader, A. A. Gabriel, C. Pelties, A. Bode, W. Barth, X. K. Liao, K. Vaidyanathan, *et al.* (2014). Petascale high order dynamic rupture earthquake simulations on heterogeneous supercomputers, in *Proc. of the International Conference for High Performance Computing, Networking, Storage and Analysis*, IEEE, 16–21 November 2014, New Orleans, Los Angeles, U.S.A., 3–15.
- Hough, S. E., E. Thompson, G. A. Parker, R. W. Graves, K. W. Hudnut, J. Patton, T. Dawson, T. Ladinsky, M. Oskin, K. Sirorattanakul, *et al.* (2020). Near-field ground motions from the July 2019 Ridgecrest, California, earthquake sequence, *Seismol. Res. Lett.* **91**, no. 3, 1542–1555.
- Hu, F., J. Wen, and X. Chen (2018). High frequency near-field ground motion excited by strike-slip step overs, *J. Geophys. Res.* **123**, no. 3, 2303–2317.
- Hu, Z., D. Roten, K. B. Olsen, and S. M. Day (2021). Modeling of empirical transfer functions with 3D velocity structure, *Bull. Seismol. Soc. Am.* **111**, no. 4, 2042–2056, doi: [10.1785/0120200214](https://doi.org/10.1785/0120200214).
- Huang, Y., J.-P. Ampuero, and D. V. Helmberger (2016). The potential for supershear earthquakes in damaged fault zones—theory and observations, *Earth Planet. Sci. Lett.* **433**, 109–115.
- Ide, S., G. C. Beroza, S. G. Prejean, and W. L. Ellsworth (2003). Apparent break in earthquake scaling due to path and site effects on deep borehole recordings, *J. Geophys. Res.* **108**, no. B5, [10.1029/2001JB001617](https://doi.org/10.1029/2001JB001617).
- Imperator, W., and P. M. Mai (2012). Broad-band near-field ground motion simulations in 3-dimensional scattering media, *Geophys. J. Int.* **192**, no. 2, 725–744.
- Jia, Z., Z. Jin, M. Marchandon, T. Ulrich, A.-A. Gabriel, W. Fan, P. Shearer, X. Zou, J. Rekoske, F. Bulut, *et al.* (2023). The complex dynamics of the 2023 Kahramanmaraş, Turkey, M_w 7.8–7.7 earthquake doublet, *Science* **381**, 985–990.
- Kagan, Y. Y., and H. Houston (2005). Relation between mainshock rupture process and Omori's law for aftershock moment release rate, *Geophys. J. Int.* **163**, no. 3, 1039–1048.
- Kaiser, A., N. Balfour, B. Fry, C. Holden, N. Litchfield, M. Gerstenberger, E. D'Anastasio, N. Horspool, G. McVerry, J. Ristau, *et al.* (2017). The 2016 Kaikōura, New Zealand, earthquake: Preliminary seismological report, *Seismol. Res. Lett.* **88**, no. 3, 727–739.
- Takehi, Y., and K. Irikura (1996). Estimation of high-frequency wave radiation areas on the fault plane by the envelope inversion of acceleration seismograms, *Geophys. J. Int.* **125**, no. 3, 892–900.
- Kanamori, H., H.-K. Thio, D. Dreger, E. Hauksson, and T. Heaton (1992). Initial investigation of the Landers, California, earthquake of 28 June 1992 using TERRAScope, *Geophys. Res. Lett.* **19**, no. 22, 2267–2270.
- Kane, D. L., P. M. Shearer, B. P. Goertz-Allmann, and F. L. Vernon (2013). Rupture directivity of small earthquakes at Parkfield, *J. Geophys. Res.* **118**, no. 1, 212–221.
- Kaneko, Y., and H. Goto (2022). The origin of large, long-period near-fault ground velocities during surface-breaking strike-slip earthquakes, *Geophys. Res. Lett.* **49**, no. 10, doi: [10.1029/2022GL098029](https://doi.org/10.1029/2022GL098029).
- Kaneko, Y., and P. M. Shearer (2014). Seismic source spectra and estimated stress drop derived from cohesive-zone models of circular subshear rupture, *Geophys. J. Int.* **197**, no. 2, 1002–1015.
- Kaneko, Y., and P. M. Shearer (2015). Variability of seismic source spectra, estimated stress drop, and radiated energy, derived from cohesive-zone models of symmetrical and asymmetrical circular and elliptical ruptures, *J. Geophys. Res.* **120**, no. 2, 1053–1079.
- Karimzadeh, S., A. Askan, and A. Yakut (2018). *Assessment of Simulated Ground Motions in Earthquake Engineering Practice: A Case Study for Duzce (Turkey)*, Springer International Publishing, Cham, Germany, 265–283.
- Kearse, J., and Y. Kaneko (2020). On-fault geological fingerprint of earthquake rupture direction, *J. Geophys. Res.* **125**, no. 9, doi: [10.1029/2020JB019863](https://doi.org/10.1029/2020JB019863).
- Kemna, K. B., A. F. Peña Castro, R. M. Harrington, and E. S. Cochran (2020). Using a large-n seismic array to explore the robustness of spectral estimations, *Geophys. Res. Lett.* **47**, no. 21, doi: [10.1029/2020GL089342](https://doi.org/10.1029/2020GL089342).
- Krenz, L., C. Uphoff, T. Ulrich, A.-A. Gabriel, L. S. Abrahams, E. M. Dunham, and M. Bader (2021). 3D acoustic-elastic coupling with gravity: The dynamics of the 2018 Palu, Sulawesi earthquake and tsunami, in *The International Conference for High Performance Computing, Networking, Storage and Analysis, SC '21*, Association for Computing Machinery, doi: [10.1145/3458817.3476173](https://doi.org/10.1145/3458817.3476173).
- Krischer, L., T. Megies, R. Barsch, M. Beyreuther, T. Lecocq, C. Caudron, and J. Wassermann (2015). ObsPy: A bridge for seismology into the scientific python ecosystem, *Comput. Sci. Discov.* **8**, no. 1, 014,003.
- Kutschera, F., A.-A. Gabriel, S. A. Wirp, B. Li, T. Ulrich, C. Abril, and B. Halldórsson (2023). Linked and fully-coupled 3D earthquake dynamic rupture and tsunami modeling for the Húsavík-Flatey fault zone in North Iceland, EGU sphere, doi: [10.5194/egu-sphere-2023-1262](https://doi.org/10.5194/egu-sphere-2023-1262).
- Langbein, J., R. Borchardt, D. Dreger, J. Fletcher, J. L. Hardebeck, M. Hellweg, C. Ji, M. Johnston, J. R. Murray, R. Nadeau, *et al.* (2005). Preliminary report on the 28 September 2004, M 6.0 Parkfield, California earthquake, *Seismol. Res. Lett.* **76**, no. 1, 10–26.
- Lee, E.-J., P. Chen, T. H. Jordan, P. B. Maechling, M. A. M. Denolle, and G. C. Beroza (2014). Full-3-D tomography for crustal structure in southern California based on the scattering-integral and the adjoint-wavefield methods, *J. Geophys. Res.* **119**, no. 8, 6421–6451.
- Li, B., A.-A. Gabriel, T. Ulrich, C. Abril, and B. Halldórsson (2023). Dynamic rupture models, fault interaction and ground motion simulations for the segmented Húsavík-Flatey fault zone, northern Iceland, *J. Geophys. Res.* **128**, no. 6, doi: [10.1029/2022JB025886](https://doi.org/10.1029/2022JB025886).
- Li, B., B. Wu, H. Bao, D. D. Oglesby, A. Ghosh, A.-A. Gabriel, L. Meng, and R. Chu (2022). Rupture heterogeneity and directivity effects in back-projection analysis, *J. Geophys. Res.* **127**, no. 3, doi: [10.1029/2021JB022663](https://doi.org/10.1029/2021JB022663).
- Li, J., T. Kim, N. Lapusta, E. Biondi, and Z. Zhan (2023). The break of earthquake asperities imaged by distributed acoustic sensing, *Nature* **620**, 800–806.
- Lindley, G. T., and R. J. Archuleta (1992). Earthquake source parameters and the frequency dependence of attenuation at Coalinga, Mammoth Lakes, and the Santa Cruz mountains, California, *J. Geophys. Res.* **97**, no. B10, 14,137–14,154.
- Liu, C., T. Lay, E. E. Brodsky, K. Dascher-Cousineau, and X. Xiong (2019). Coseismic rupture process of the large 2019 Ridgecrest earthquakes from joint inversion of geodetic and seismological observations, *Geophys. Res. Lett.* **46**, 11,820–11,829.

- Liu, M., Y. Huang, and J. Ritsema (2023). Characterizing multisubevent earthquakes using the Brune source model, *Bull. Seismol. Soc. Am.* **113**, no. 2, 577–591.
- Lozos, J. C., D. D. Oglesby, J. N. Brune, and K. B. Olsen (2014). Rupture propagation and ground motion of strike-slip Stepovers with intermediate fault segments, *Bull. Seismol. Soc. Am.* **105**, no. 1, 387–399.
- Madariaga, R. (1976). Dynamics of an expanding circular fault, *Bull. Seismol. Soc. Am.* **66**, 639–666.
- Madariaga, R. (1977). High-frequency radiation from crack (stress drop) models of earthquake faulting, *Geophys. J. Int.* **51**, no. 3, 625–651.
- Madariaga, R. (1983). High frequency radiation from dynamic earthquake fault models, *Ann. Geophys.* **1**, 17–23.
- Madariaga, R. (2015). Seismic source theory, in *Treatise on Geophysics*, Second Edn., Elsevier, 51–71.
- Madariaga, R., J. P. Ampuero, and M. Adda-Bedia (2006). Seismic radiation from simple models of earthquakes, AGU, Geophysical Monograph Series, 170, doi: [10.1029/170GM23](https://doi.org/10.1029/170GM23).
- Madariaga, R., S. Ruiz, E. Rivera, F. Leyton, and J. Baez (2019). Near-field spectra of large earthquakes, *Pure Appl. Geophys.* **176**, 983–1001.
- Marty, S., F. X. Passelègue, J. Aubry, H. S. Bhat, A. Schubnel, and R. Madariaga (2019). Origin of high-frequency radiation during laboratory earthquakes, *Geophys. Res. Lett.* **46**, no. 7, 3755–3763.
- Milliner, C. W. D., J. F. Dolan, J. Hollingsworth, S. Leprince, F. Ayoub, and C. G. Sammis (2015). Quantifying near-field and off-fault deformation patterns of the 1992 M_w 7.3 Landers earthquake, *Geochem. Geophys. Geosys.* **16**, no. 5, 1577–1598.
- Niu, Z., A.-A. Gabriel, L. Seelinger, and H. Igel (2023). Modeling and quantifying parameter uncertainty of co-seismic non-classical nonlinearity in rocks, available at <https://arxiv.org/abs/2306.04197> (last accessed November 2023).
- Oeser, J., H.-P. Bunge, and M. Mohr (2006). Cluster design in the earth sciences Tethys, in *High Performance Computing and Communications*, M. Gerndt and D. Kranzlmüller (Editors), Springer Berlin, Heidelberg, Germany, 31–40.
- Oglesby, D. D., and P. M. Mai (2012). Fault geometry, rupture dynamics and ground motion from potential earthquakes on the north Anatolian fault under the Sea of Marmara, *Geophys. J. Int.* **188**, no. 3, 1071–1087.
- Oglesby, D. D., R. J. Archuleta, and S. B. Nielsen (1998). Earthquakes on dipping faults: The effects of broken symmetry. *Science* **280**, no. 5366, 1055–1059.
- Oglesby, D. D., R. J. Archuleta, and S. B. Nielsen (2000). The three-dimensional dynamics of dipping faults, *Bull. Seismol. Soc. Am.* **90**, no. 3, 616–628.
- Okuwaki, R., Y. Yagi, and S. Hirano (2014). Relationship between high-frequency radiation and asperity ruptures, revealed by hybrid back-projection with a non-planar fault model, *Sci. Rep.* **4**, 7120.
- Olsen, K., S. Day, B. Minster, Y. Cui, A. Chourasia, D. Okaya, P. Maechling, and T. Jordan (2008). TeraShake2: Spontaneous rupture simulations of M_w 7.7 earthquakes on the southern San Andreas fault, *Bull. Seismol. Soc. Am.* **98**, 1162–1185.
- Olsen, K. B., S. M. Day, and C. R. Bradley (2003). Estimation of Q for long-period (> 2 sec) waves in the Los Angeles basin, *Bull. Seismol. Soc. Am.* **93**, no. 2, 627–638.
- Paziewski, J., G. Kurpinski, P. Wielgosz, L. Stolecki, R. Sieradzki, M. Seta, S. Oszczak, M. Castillo, and F. PorquerasMartin- (2020). Towards Galileo + GPS seismology: Validation of high-rate GNSS-based system for seismic events characterization, *Measurement* **166**, 108,236.
- Pelties, C., A.-A. Gabriel, and J.-P. Ampuero (2014). Verification of an ADER-DG method for complex dynamic rupture problems, *Geosci. Model Dev.* **7**, no. 3, 847–866.
- Pelties, C., J. D. la Puente, J.-P. Ampuero, G. Brietzke, and M. Käser (2012). Three-dimensional dynamic rupture simulation with a high-order discontinuous Galerkin method on unstructured tetrahedral meshes, *J. Geophys. Res.* **117**, doi: [10.1029/2011JB008857](https://doi.org/10.1029/2011JB008857).
- Pennington, C. N., Q. Wu, X. Chen, and R. E. Abercrombie (2023). Quantifying rupture characteristics of microearthquakes in the Parkfield area using a high-resolution borehole network, *Geophys. J. Int.* **233**, no. 3, 1772–1785.
- Pitarka, A., A. Akinci, P. GoriDe, and M. Buttinelli (2021). Deterministic 3D ground-motion simulations (0–5 Hz) and surface topography effects of the 30 October 2016 M_w 6.5 Norcia, Italy, earthquake, *Bull. Seismol. Soc. Am.* **112**, no. 1, 262–286, doi: [10.1785/0120210133](https://doi.org/10.1785/0120210133).
- Pulido, N., and L. A. Dalguer (2009). Estimation of the high-frequency radiation of the 2000 Tottori (Japan) earthquake based on a dynamic model of fault rupture: Application to the strong ground motion simulation, *Bull. Seismol. Soc. Am.* **99**, no. 4, 2305–2322.
- Ripperger, J., P. M. Mai, and J.-P. Ampuero (2008). Variability of near-field ground motion from dynamic earthquake rupture simulations, *Bull. Seismol. Soc. Am.* **98**, no. 3, 1207–1228.
- Rodgers, A. J., N. Anders Petersson, A. Pitarka, D. B. McCallen, B. Sjogreen, and N. Abrahamson (2019). Broadband (0–5 Hz) fully deterministic 3D ground-motion simulations of a magnitude 7.0 Hayward fault earthquake: Comparison with empirical ground-motion models and 3D path and site effects from source normalized intensities, *Seismol. Res. Lett.* **90**, no. 3, 1268–1284.
- Ross, Z. E., B. Idini, Z. Jia, O. L. Stephenson, M. Zhong, X. Wang, Z. Zhan, M. Simons, E. J. Fielding, S.-H. Yun, et al. (2019). Hierarchical interlocked orthogonal faulting in the 2019 Ridgecrest earthquake sequence, *Science* **366**, no. 6463, 346–351.
- Rost, S., and C. Thomas (2002). Array seismology: Methods and applications, *Rev. Geophys.* **40**, no. 3, 2-1–2-27.
- Roten, D., K. B. Olsen, and S. M. Day (2017). Off-fault deformations and shallow slip deficit from dynamic rupture simulations with fault zone plasticity, *Geophys. Res. Lett.* **44**, no. 15, 7733–7742.
- Roten, D., T. Yeh, K. B. Olsen, S. M. Day, and Y. Cui (2023). Implementation of Iwan-type nonlinear rheology in a 3D high-order staggered-grid finite-difference method, *Bull. Seismol. Soc. Am.* doi: [10.1785/0120230011](https://doi.org/10.1785/0120230011).
- Savran, W. H., and K. B. Olsen (2020). Kinematic rupture generator based on 3-D spontaneous rupture simulations along geometrically rough faults, *J. Geophys. Res.* **125**, no. 10, doi: [10.1029/2020JB019464](https://doi.org/10.1029/2020JB019464).
- Schmedes, J., R. J. Archuleta, and D. Lavallée (2010). Correlation of earthquake source parameters inferred from dynamic rupture simulations, *J. Geophys. Res.* **115**, no. B3, doi: [10.1029/2009JB006689](https://doi.org/10.1029/2009JB006689).
- Shakal, A., H. Haddadi, V. Graizer, K. Lin, and M. Huang (2006). Some key features of the strong-motion data from the M 6.0 Parkfield, California, earthquake of 28 September 2004, *Bull. Seismol. Soc. Am.* **96**, no. 4B, S90–S118.

- Shaw, J. H., A. Plesch, C. Tape, M. P. Suess, T. H. Jordan, G. Ely, E. Hauksson, J. Tromp, T. Tanimoto, R. Graves, *et al.* (2015). Unified structural representation of the southern California crust and upper mantle, *Earth Planet. Sci. Lett.* **415**, 1–15.
- Shi, Z., and S. M. Day (2013). Rupture dynamics and ground motion from 3-D rough-fault simulations, *J. Geophys. Res.* **118**, no. 3, 1122–1141.
- Sieh, K., L. Jones, E. Hauksson, K. Hudnut, D. Eberhart-Phillips, T. Heaton, S. Hough, K. Hutton, H. Kanamori, A. Lilje, *et al.* (1993). Near-field investigations of the landers earthquake sequence, April to July 1992, *Science* **260**, no. 5105, 171–176.
- Small, P., D. Gill, P. Maechling, R. Taborda, S. Callaghan, T. Jordan, K. Olsen, G. Ely, and C. Goulet (2017). The SCEC unified community velocity model software framework, *Seismol. Res. Lett.* **88**, 1539–1552.
- Somerville, P. G., N. F. Smith, R. W. Graves, and N. A. Abrahamson (1997). Modification of empirical strong ground motion attenuation relations to include the amplitude and duration effects of rupture directivity, *Seismol. Res. Lett.* **68**, no. 1, 199–222.
- Spudich, P., and B. S. J. Chiou (2008). Directivity in NGA earthquake ground motions: Analysis using isochrone theory, *Earthq. Spectra* **24**, no. 1, 279–298.
- Spudich, P., and E. Cranswick (1984). Direct observation of rupture propagation during the 1979 Imperial Valley earthquake using a short baseline accelerometer array, *Bull. Seismol. Soc. Am.* **74**, no. 6, 2083–2114.
- Spudich, P., and L. N. Frazer (1984). Use of ray theory to calculate high-frequency radiation from earthquake sources having spatially variable rupture velocity and stress drop, *Bull. Seismol. Soc. Am.* **74**, no. 6, 2061–2082.
- Stein, S., and M. Wysession (2003). *An Introduction to Seismology, Earthquakes, and Earth*, Blackwell Science, Oxford, doi: [10.1017/S0016756803318837](https://doi.org/10.1017/S0016756803318837).
- Strasser, F. O., and J. J. Bommer (2009). Large-amplitude ground-motion recordings and their interpretations, *Soil Dynam. Earthq. Eng.* **29**, no. 10, 1305–1329.
- Takemura, S., T. Furumura, and T. Maeda (2015). Scattering of high-frequency seismic waves caused by irregular surface topography and small-scale velocity inhomogeneity, *Geophys. J. Int.* **201**, no. 1, 459–474.
- Takemura, S., T. Furumura, and T. Saito (2009). Distortion of the apparent S-wave radiation pattern in the high-frequency wavefield: Tottori-Ken Seibu, Japan, earthquake of 2000, *Geophys. J. Int.* **178**, no. 2, 950–961.
- Taufiqurrahman, T., A.-A. Gabriel, D. Li, T. Ulrich, B. Li, S. Carena, A. Verdecchia, and F. Gallovič (2023). Dynamics, interactions and delays of the 2019 Ridgecrest rupture sequence, *Nature* **618**, 308–315.
- Taufiqurrahman, T., A.-A. Gabriel, T. Ulrich, L. Valentová, and F. Gallovič (2022). Broadband dynamic rupture modeling with fractal fault roughness, frictional heterogeneity, viscoelasticity and topography: The 2016 M_w 6.2 Amatrice, Italy earthquake, *Geophys. Res. Lett.* doi: [10.1029/2022GL098872](https://doi.org/10.1029/2022GL098872).
- Thatcher, W., and T. C. Hanks (1973). Source parameters of southern California earthquakes, *J. Geophys. Res.* **78**, no. 35, 8547–8576.
- Tinti, E., P. Spudich, and M. Cocco (2005). Earthquake fracture energy inferred from kinematic rupture models on extended faults, *J. Geophys. Res.* **110**, no. B12, doi: [10.1029/2005JB003644](https://doi.org/10.1029/2005JB003644).
- Trugman, D. T. (2020). Stress-drop and source scaling of the 2019 Ridgecrest, California, earthquake sequence, *Bull. Seismol. Soc. Am.* **110**, no. 4, 1859–1871.
- Trugman, D. T., S. X. Chu, and V. C. Tsai (2021). Earthquake source complexity controls the frequency dependence of near-source radiation patterns, *Geophys. Res. Lett.* **48**, no. 17, doi: [10.1029/2021GL095022](https://doi.org/10.1029/2021GL095022).
- Ulrich, T., A. Gabriel, J. P. Ampuero, and W. Xu (2019). Dynamic viability of the 2016 M_w 7.8 Kaikōura earthquake cascade on weak crustal faults, *Nat. Commun.* **10**, 1213.
- Ulrich, T., S. Vater, E. H. Madden, J. Behrens, Y. Dinthervan, I. van Zelst, E. J. Fielding, C. Liang, and A.-A. Gabriel (2019). Coupled, physics-based modeling reveals earthquake displacements are critical to the 2018 Palu, Sulawesi tsunami, *Pure Appl. Geophys.* **176**, no. 10, 4069–4109.
- Umeda, Y. (1990). High-amplitude seismic waves radiated from the bright spot of an earthquake, *Tectonophysics* **175**, no. 1, 81–92.
- Uphoff, C., and M. Bader (2016). Generating high performance matrix kernels for earthquake simulations with viscoelastic attenuation, in *Proc. of the 2016 International Conf. on High Performance Computing and Simulation*, IEEE, 908–916, doi: [10.1109/HPCSim.2016.7568431](https://doi.org/10.1109/HPCSim.2016.7568431).
- Uphoff, C., S. Rettenberger, M. Bader, E. H. Madden, T. Ulrich, S. Wollherr, and A.-A. Gabriel (2017). Extreme scale multi-physics simulations of the tsunamigenic 2004 Sumatra megathrust earthquake, in *Proc. of the International Conf. for High Performance Computing, Networking, Storage and Analysis*, ACM, 21, doi: [10.1145/3126908.3126948](https://doi.org/10.1145/3126908.3126948).
- Vallée, M., and V. Douet (2016). A new database of source time functions (STFs) extracted from the SCARDEC method, *Phys. Earth Planet. In.* **257**, 149–157.
- Verdecchia, A., and S. Carena (2016). Coulomb stress evolution in a diffuse plate boundary: 1400 years of earthquakes in eastern California and western Nevada, USA, *Tectonics* **35**, no. 8, 1793–1811.
- Virtanen, P., R. Gommers, T. E. Oliphant, M. Haberland, T. Reddy, D. Cournapeau, E. Burovski, P. Peterson, W. Weckesser, J. Bright, *et al.* (2020). SciPy 1.0: Fundamental algorithms for scientific computing in Python, *Nat. Methods* **17**, 261–272.
- Vyas, J. C., A. Gabriel, T. Ulrich, P. M. Mai, and J. Ampuero (2023). How does thermal pressurization of pore fluids affect 3D strike-slip earthquake dynamics and ground motions? *Bull. Seismol. Soc. Am.* **13**, 1992–2008.
- Wang, Y., and S. M. Day (2017). Seismic source spectral properties of crack-like and pulse-like modes of dynamic rupture, *J. Geophys. Res.* **122**, no. 8, 6657–6684.
- Wang, Y., and S. M. Day (2020). Effects of off-fault inelasticity on near-fault directivity pulses, *J. Geophys. Res.* **125**, no. 7, doi: [10.1029/2019JB019074](https://doi.org/10.1029/2019JB019074).
- Withers, K. B., K. B. Olsen, S. M. Day, and Z. Shi (2018). Ground motion and intraevent variability from 3D deterministic broadband (0–7.5 Hz) simulations along a nonplanar strike-slip fault, *Bull. Seismol. Soc. Am.* **109**, no. 1, 229–250.
- Wolf, S., A.-A. Gabriel, and M. Bader (2020). Optimization and local time stepping of an ADER-DG scheme for fully anisotropic wave propagation in complex geometries, in *Computational Science—ICCS 2020, Lecture Notes in Computer Science*, Springer International Publishing, Cham, Germany, 32–45.

- Wolf, S., M. Galis, C. Uphoff, A.-A. Gabriel, P. Moczo, D. Gregor, and M. Bader (2022). An efficient ADER-DG local time stepping scheme for 3D HPC simulation of seismic waves in poroelastic media, *J. Comput. Phys.* **455**, 110,886.
- Wollherr, S., A.-A. Gabriel, and C. Uphoff (2018). Implementation, verification and application of off-fault plasticity in three-dimensional dynamic rupture simulations on complex fault geometries using a modal discontinuous Galerkin method, *Geophys. J. Int.* **214**, 1556–1584.
- Wollherr, S., A.-A. Gabriel, and P. M. Mai (2019). Landers 1992 “Reloaded”: Integrative dynamic earthquake rupture modeling, *J. Geophys. Res.* **124**, 6666–6702.
- Yamashita, T., and Y. Umeda (1994). Earthquake rupture complexity due to dynamic nucleation and interaction of subsidiary faults, *Pure Appl. Geophys.* **143**, no. 1, 89–116.
- Yang, W., and E. Hauksson (2013). The tectonic crustal stress field and style of faulting along the Pacific North America plate boundary in southern California, *Geophys. J. Int.* **194**, no. 1, 100–107.
- Yeh, T., and K. B. Olsen (2023). Fault damage zone effects on ground motions during the 2019 M_w 7.1 Ridgecrest, California, earthquake, *Bull. Seismol. Soc. Am.* **113**, no. 4, 1724–1738, doi: [10.1785/0120220249](https://doi.org/10.1785/0120220249).
- Yoshida, K., and H. Kanamori (2023). Time-domain source parameter estimation of M_w 3–7 earthquakes in Japan from a large database of moment-rate functions, *Geophys. J. Int.* **234**, no. 1, 243–262.
- Yu, Z., Q. Liu, J. Xu, and X. Chen (2022). Simulation of dynamic rupture process and near-field strong ground motion for the Wenchuan earthquake, *Bull. Seismol. Soc. Am.* **112**, 2828–2846, doi: [10.1785/0120220041](https://doi.org/10.1785/0120220041).
- Zeng, Y., K. Aki, and T.-L. Teng (1993). Mapping of the high-frequency source radiation for the Loma Prieta earthquake, California, *J. Geophys. Res.* **98**, no. B7, 11,981–11,993.
- Zhan, Z. (2019). Distributed acoustic sensing turns fiber-optic cables into sensitive seismic antennas, *Seismol. Res. Lett.* **91**, no. 1, 1–51.
- Zhang, H., and Z. Ge (2017). Stepped rupture of the 2014 M_w 7.0 Yutian, Xinjiang, earthquake, *Bull. Seismol. Soc. Am.* **107**, no. 2, 581–591.

Appendix

3D dynamic rupture models

The TPV5 U.S. Geological Survey (USGS)/Southern California Earthquake Center (SCEC) dynamic rupture community benchmark (Harris *et al.*, 2009) describes a bilateral strike-slip earthquake in 3D dynamically propagating across a rectangular fault that intersects the free surface in an elastic half-space. The rupture is artificially nucleated in the middle of the fault and then spreads spontaneously in each direction. To the left or right of its center, the model setup includes an asperity and a barrier with elevated or reduced initial shear stresses, which accelerate or decelerate dynamic rupture, respectively. The rupture is forced to stop abruptly at the fault edges. The dynamic model parameters are summarized in Table A1.

Wollherr *et al.* (2019) developed a 3D dynamic rupture model of the 1992 M_w 7.3 Landers earthquake that includes

TABLE A1

Summary of the TPV5 Dynamic Rupture Model Parameters (See Data and Resources; Harris *et al.*, 2009)

Symbol	Parameter	Value
μ_s	Static friction	0.677
μ_d	Dynamic friction	0.525
D_c	Critical slip-weakening distance	0.4 m
Cohesion	Frictional cohesion	0.0 MPa
S_{yy}	Stress	120 MPa
$S_{xx}, S_{zz}, S_{yz}, S_{xz}$	Stress	0 MPa
S_{xy}	Stress outside the nucleation zone	70 MPa
	Stress inside the nucleation zone	81.6 MPa
	Stress inside the barrier	62 MPa
	Stress inside the asperity	78 MPa

geometric fault complexity and matches a broad range of regional and local observations, including fault slip, seismic moment release, and ground motions (Fig. 7). The dynamic rupture earthquake model uses a linear slip-weakening friction law, high-resolution topography, 3D velocity structure (CVM-H; Shaw *et al.*, 2015), viscoelastic attenuation, and off-fault (visco-)plasticity. Q values are proportional to the S-wave velocity as $Q_S = 0.05V_S$ and $Q_P = 2Q_S$ (Graves *et al.*, 2008). The fault system of the Landers dynamic rupture model consists of five vertical subfaults that extend to a depth of 15 km, adapted from fault traces from photometric images (Fleming *et al.*, 1998). The fault system exhibits a strike rotation of $\sim 30^\circ$, striking toward the north in the southern part and toward the northwest in the northern part. Wollherr *et al.* (2019) find that assuming a constant maximum principal stress direction inhibits rupture propagation across the fault system. In their setup, the maximum principal stress axis varies smoothly, which is consistent with the regional stress estimates. Dynamic rupture is initiated by gradually reducing the static friction coefficient to its dynamic value within a circular nucleation patch of radius 1.5 km (Bizzarri, 2010). Table A2 provides an overview of all model parameters.

Taufiqurrahman *et al.* (2023) modeled linked foreshock–mainshock dynamic rupture scenarios of the 2019 Ridgecrest sequence, the M_w 6.4 Searles Valley foreshock, and the M_w 7.1 Ridgecrest mainshock. Their dynamic rupture scenario assembles earthquake physics with high-quality strong-motion and teleseismic, field mapping, high-rate Global Navigation Satellite Systems (GNSS), and space geodetic foreshock and mainshock data sets of California’s largest earthquakes for 20 yr. The initial 3D stress state is inferred from tectonic background loading (Yang and Hauksson, 2013), which is

TABLE A2

Summary of the Landers Dynamic Rupture Model Parameters (Adapted from table 1 in Wollherr *et al.*, 2019)

Symbol	Parameter	Value with Units
μ_s	Static friction	0.55 (0.44 at the Emmerson fault and Camp Rock fault)
μ_d	Dynamic friction	0.22
D_c	Critical slip distance	0.62 m
C	Bulk cohesion	Depth-dependent, good quality rock model of Roten <i>et al.</i> (2017) ranging between 2.5 and 50.0 MPa
ϕ	Friction angle	0.55
V_S, V_P	Shear- and P -wave velocity	3D CVM-H model Shaw <i>et al.</i> (2015)
ρ	Density	3D CVM-H model Shaw <i>et al.</i> (2015)
Q_S, Q_P	Viscoelastic damping parameters	50 V_S , 2 Q_S
R	Nucleation patch radius	1.5 km
	Forced nucleation time	0.6 s
R	Relative prestress ratio	0.65
σ_2	Principal vertical stress	(2700–1000) kg/m 9.8 abs (depth m)
σ_1, σ_3	Principal horizontal stresses	Amplitudes determined by R and equations (2) and (3) in Wollherr <i>et al.</i> (2019)
dx	Smallest element edge	200 m
p	Polynomial order of accuracy	4

additionally modulated by long-term Coulomb failure stress changes (Δ CFS) caused by previous major earthquakes in the eastern California shear zone ([Verdecchia and Carena, 2016](#)). The prestress of the mainshock dynamic rupture scenario includes stress changes induced by the foreshock. Although a realistic dynamic rupture scenario of the Ridgecrest mainshock needs to account for the stress changes due to the Searles Valley foreshock, the foreshock does not dynamically trigger the mainshock. The models include viscoelastic attenuation, off-fault plasticity, and a nonvertical quasi-orthogonal 3D fault system with four fault segments (Fig. 3). [Taufiqurrahman *et al.* \(2023\)](#) construct the fault system geometry by integrating geological field mapping, geodetic

TABLE A3

Rate-and-State Frictional Fault Properties of the Ridgecrest Sequence Models (Adapted from table S2 in [Taufiqurrahman *et al.*, 2023](#))

Parameter	Symbol	Value
Direct-effect parameter	a	0.01–0.02
Evolution-effect parameter	b	0.014
Reference slip rate	V_0	10^{-6} m/s
Steady-state low-velocity friction coefficient at the slip rate V_0	f_0	0.6
Characteristic slip distance of the state evolution	L	0.2
Full weakened friction coefficient	f_w	0.1
Initial slip rate	V_{ini}	10^{-16} m/s
Weakened slip rate	V_w	0.1 m/s

Interferometric Synthetic Aperture Radar data, relocated seismicity, and selected focal mechanisms ([Carena and Suppe, 2002](#)). The fault system is embedded into a 3D velocity model of southern California (CVM-S4.26; [Lee *et al.*, 2014](#); [Small *et al.*, 2017](#)) and intersects high-resolution topography. Q values are coupled to the velocity structure as $Q_S = 0.1V_S$ and $Q_P = 1.5Q_S$ ([Olsen *et al.*, 2003](#)). Table A3 summarizes the frictional fault properties. Both ruptures are nucleated by imposing shear stress perturbations in spherical nucleation areas with radii of 3.5 km around their respective hypocenters.

All dynamic rupture simulations use the open-source software package SeisSol (see [Data and Resources](#)) to solve the problem of spontaneous frictional failure on prescribed faults and nonlinearly coupled seismic wave propagation. SeisSol uses the arbitrary high-order accurate derivative discontinuous Galerkin (ADER-DG) method and employs fully adaptive, unstructured tetrahedral meshes ([Dumbser and Käser, 2006](#); [de la Puente *et al.*, 2009](#); [Pelties *et al.*, 2012](#)). Tetrahedral elements enable meshing flexibility and are crucial to incorporate complex and intersecting geometries such as those inherent to the Ridgecrest and Landers fault systems. SeisSol is verified in a variety of dynamic rupture benchmark problems ([Pelties *et al.*, 2014](#); [Harris *et al.*, 2018](#)) and is optimized to efficiently exploit high-performance computing infrastructures (e.g., [Breuer *et al.*, 2014](#); [Uphoff *et al.*, 2017](#); [Krenz *et al.*, 2021](#)). SeisSol supports high computational efficiency when incorporating elastic, anisotropic, viscoelastic, viscoplastic, and poroelastic rheologies ([Uphoff and Bader, 2016](#); [Wollherr *et al.*, 2018](#); [Wolf *et al.*, 2020, 2022](#)). The Landers and Ridgecrest dynamic rupture earthquake scenarios account for off-fault (visco)plasticity and viscoelastic attenuation. Within our here-considered model domains, the seismic wavefield is resolved up to at least 1 Hz in the TPV5 and Landers models and up to 2 Hz in the

Ridgecrest dynamic rupture simulations. Synthetic spectra of an underresolved numerical model would deviate from the typical ω^2 decay (Figs. S5 and S6, Wollherr *et al.*, 2019). The TPV5 dynamic rupture model requires 2000 central processing unit (CPU) hours on the supercomputer Supermuc-NG, the Landers earthquake scenarios require $\sim 100,000$ CPU hours on Supermuc Phase-2, and the linked simulation of the Ridgecrest sequence requires 243,000 CPU hours on Supermuc-NG.

On near-field effects

There exist different approaches to separate far- from near-field effects. The ratio of the distance to the source, R , and the examined seismic wavelength, λ , can determine the

relevance of near-field terms (i.e., static displacements). If $R/\lambda \gg 1$, near-field terms are negligible (Madariaga, 2015). In addition, the relevance of source finiteness is considered to be large when the ratio of earthquake rupture duration T_R and the examined seismic wave period T (T_R/T) is large (Stein and Wysession, 2003). Our dynamic rupture scenarios include regions where near-field terms are negligible. However, within the analyzed frequency ranges, the waveforms are generally expected to be affected by finite-source effects within the considered model domains.

Manuscript received 10 July 2023
Published online 7 December 2023